UC Santa Barbara

UC Santa Barbara Previously Published Works

Title

Local Structure Evolution and Modes of Charge Storage in Secondary Liâ��FeS 2 Cells

Permalink

https://escholarship.org/uc/item/8st7560d

Journal

Chemistry of Materials, 29(7)

ISSN

0897-4756 1520-5002

Authors

Butala, Megan M
Mayo, Martin
Doan-Nguyen, Vicky V. T
et al.

Publication Date

2017-03-27

DOI

10.1021/acs.chemmater.7b00070

Peer reviewed

eScholarship.org Powered by the California Digital Library
University of California

Local Structure Evolution and Modes of Charge Storage in Secondary Li–FeS_2 Cells

Megan M. Butala,[*,†] Martin Mayo,[‡] Vicky V. T. Doan-Nguyen,[¶] Margaret A. Lumley,[†,§] Claudia Göbel,[†] Kamila M. Wiaderek,[‖] Olaf J. Borkiewicz,[‖] Karena W. Chapman,[‖] Peter J. Chupas,[‖] Mahalingam Balasubramanian,[‖] Geneva Laurita,[†] Sylvia Britto,[⊥] Andrew J. Morris,[*,‡] Clare P. Grey,[*,⊥] and Ram Seshadri[*,†,§]

†*Mitsubishi Chemical Center for Advanced Materials, Materials Department, and Materials Research Laboratory, University of California, Santa Barbara, CA 93106, United States*

‡*Theory of Condensed Matter Group, Cavendish Laboratory, University of Cambridge, Cambridge CB3 0HE, United Kingdom*

¶*California NanoSystems Institute, University of California, Santa Barbara, CA 93106, United States*

§*Department of Chemistry and Biochemistry, University of California, Santa Barbara, CA 93106, United States*

‖*X-ray Science Division, Advanced Photon Source, Argonne National Laboratory, Argonne, IL 60439, United States*

⊥*Department of Chemistry, University of Cambridge, Cambridge CB2 1EW, United Kingdom*

E-mail: mbutala@umail.ucsb.edu; ajm255@cam.ac.uk; cpg27@cam.ac.uk; seshadri@mrl.ucsb.edu

Abstract

In the pursuit of high capacity electrochemical energy storage, a promising domain of research involves conversion reaction schemes, wherein electrode materials are fully transformed during charge and discharge. There are, however, numerous difficulties in realizing theoretical capacity and high rate capability in many conversion schemes. Here we employ *operando* studies to understand the conversion material FeS_2, focusing on the local structure evolution of this relatively reversible material. X-ray absorption spectroscopy, pair distribution function analysis, and first principles calculations of intermediate structures shed light on the mechanism of charge storage in the $Li-FeS_2$ system, with some general principles emerging for charge storage in chalcogenide materials. Focusing on second and later charge/discharge cycles, we find small, disordered domains that locally resemble Fe and Li_2S at the end of the first discharge. Upon charge, this is converted to a Li-Fe-S composition whose local structure reveals tetrahedrally-coordinated Fe. With continued charge, this ternary composition displays insertion-extraction behavior at higher potentials and lower Li content. The finding of hybrid modes of charge storage, rather than simple conversion, points to the important role of intermediates that appear to store charge by mechanisms that more closely resemble intercalation.

Introduction

Detailed mechanistic understanding of the processes associated with the intercalation cathode material $LiCoO_2$ and related layered transition metal oxides has been essential to the development of modern Li-ion batteries.[1] In contrast, conversion reaction-based schemes for Li-ion batteries have not advanced as rapidly.[2,3] Conversion reaction batteries involve electrodes that are not topochemical in their mode of charge storage and instead undergo dramatic structural and compositional changes during cycling. The broad range of chemistries (including oxides, fluorides, and sulfides) and structures capable of storing charge by conversion make it difficult to elucidate mechanistic trends that are applicable across the many candidate materials.

A general trend of conversion systems is the first discharge reaction, which can be considered for a transition metal (*M*) anion (*X*) compound as (Equation 1):

$$M_aX_b + (bn)\text{Li}^+ + (bn)\text{e}^- \rightarrow aM^0 + b\text{Li}_nX \quad (1)$$

Another established phenomenon in conversion systems is the significant nanostructuring that accompanies the phase changes during the first discharge.[4,5] The formation of new interfaces during the first discharge is accompanied by a large overpotential and results in cycling products with limited long-range order, if any. The disordered nature of products contributes to the difficulty of elucidating the mechanism of charge storage and makes average structure methods, including X-ray diffraction (XRD), ill-suited to the study of conversion systems.[6,7] Rather, local structure methods, including pair distribution function (PDF) analysis and X-ray absorption spectroscopy (XAS), are powerful in studying such systems.[8–10] A number of studies applying PDF to Fe-based conversion electrode materials have greatly contributed to the mechanistic understanding of conversion systems.[4,5,11–13] In particular, *operando* characterization provides valuable information about the charge storage mechanism as the chemistry is occurring.

FeS_2 has compelling performance relative to other conversion materials, including transition metal oxides, and was originally investigated as a cathode for high temperature batteries with molten salt electrolytes.[14,15] It was later studied for room temperature secondary batteries with organic electrolytes,[16,17] with a focus on the mechanism of charge storage. A primary $Li-FeS_2$ battery has since been commercialized by Energizer.[18] Recent work by Shao-Horn and coworkers revisited earlier mechanistic studies.[19] Near-theoretical storage by FeS_2 in an all-solid state cell operating at 60°C has been reported recently,[20] as have cells based on ionic liquid electrolytes.[21]

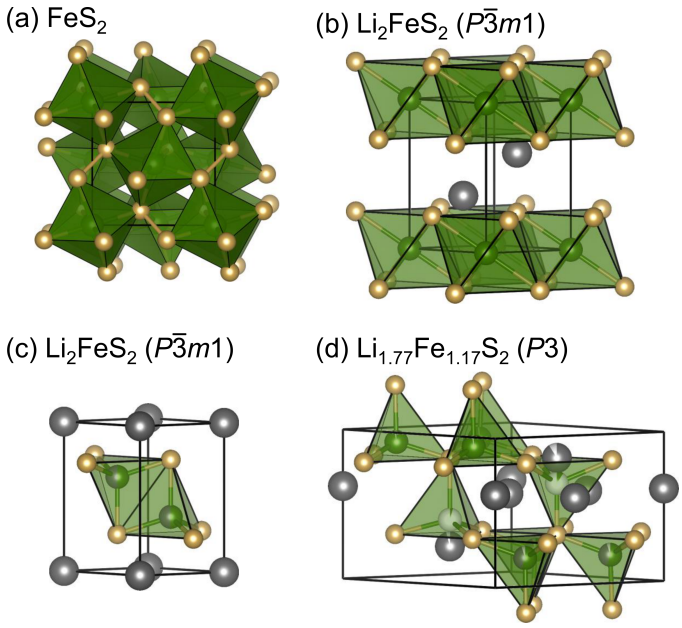

Figure 1: (a) FeS_2 ($Pa\bar{3}$) consists of a *fcc* lattice of Fe atoms (green) octahedrally-coordinated by disulfides, highlighted in yellow. Published $Li-Fe-S$ ternary phases proposed to be intermediate products during the cycling of FeS_2: (b) Li_2FeS_2 ($P\bar{3}m1$) with layers of FeS_6 octahedra with Li (grey) in tetrahedral sites between the layers,[17] (c) Li_2FeS_2 ($P\bar{3}m1$) with layers of mixed occupancy Li and Fe tetrahedrally-coordinated by S,[22] and (d) $Li_{1.77}Fe_{1.17}S_2$ ($P3$) with mixed and partial occupancy (white) of Li and Fe in corner-sharing tetrahedra.[23]

In pyrite FeS_2, Fe^{2+} forms a face-centered cubic lattice with each Fe octahedrally-coordinated by disulfide bonds of the form S_2^{2-} [Figure 1(a)]. FeS_2 can theoretically store 4 mol Li per formula unit, with a complete first discharge (Equation 2):

$$FeS_2 + 4\,Li^+ + 4\,e^- \rightarrow Fe^0 + 2\,Li_2S \quad (2)$$

FeS_2 is not recovered on charge at room temperature,[24] and consequently Equation 2 is representative of only the very first discharge. With some exceptions,[9] including for FeS_2,[25] mechanistic studies of conversion materials have typically focused on the first discharge or first cycle.[19,26,27] The first discharge cycle is unique from subsequent cycles and consequently, monitoring structural evolution after the first discharge is essential to elucidating processes representative of battery performance.

For FeS_2, there is near consensus that an intermediate phase forms during cycling. Pyrrhotite and other off-stoichiometry binaries are among those proposed,[27–29] while other literature suggests a ternary Li−Fe−S intermediate stable over a range of Li compositions.[24,25,30] Among the postulated ternary intermediates are those with layers of FeS_6 octahedra with Li in the Van der Waals gap [Figure 1(b)],[17,31] layers of Li and Fe tetrahedrally-coordinated by S between layers of LiS_6 octahedra [Figure 1(c)],[22] or a three-dimensionally connected, disordered structure with mixed and partial occupancies of Li and Fe tetrahedrally-coordinated by S [Figure 1(d)].[23]

We report new mechanistic and structural information about the reaction of FeS_2 with Li based on *operando* and *ex-situ* local structure methods. The nature of the local structure of products at various states of charge is consistent from complementary *operando* PDF and *ex-situ* XAS data. Ternary structures predicted by first principles calculations are in good agreement with the PDF data of intermediate and charge products. The mechanism(s) of charge storage for FeS_2 depend(s) on cycling conditions including rate, temperature, and electrolyte. We focus on later cycles, as stated earlier, and find for the applied conditions dual mechanisms including (i) conversion between small, disordered domains that locally resemble Fe and Li_2S and a Li−Fe−S ternary local structure with tetrahedrally-coordinated Fe at low potentials and high Li content and (ii) insertion-extraction behavior of the ternary structure at high potentials and low Li content.

Experimental and theoretical methods

Ex-situ cell assembly, cycling, and sample preparation

Cycling was carried out in Swagelok cells with loose-powder electrodes of FeS_2 (Alpha Aesar, 99.9%) and conductive carbon additive Ketjen Black (KB) (AkzoNobel EC-600JD) in a 9:1 ratio by weight. Powders were ground in air with an agate mortar and pestle. 1 M $LiPF_6$ in ethylene carbonate:dimethyl carbonate (EC:DMC) (1:1 ratio by volume) electrolyte and two Whatman glass filter dryer (GFD) separators were used. Li metal served as both the counter and reference electrode in these half-cells. Cells were assembled in an Ar-filled glove box and cycled galvanostatically at a rate of $C/40$ ($Q/10$), calculated for the theoretical reaction of FeS_2 with 4 mol Li (per formula unit) in 40 h, with potential limitations of 1 V and 3 V for discharge and charge, respectively. Cells were cycled using a Bio-Logic VMP-3.

For *ex-situ* total scattering and X-ray absorption spectroscopy (XAS), loose-powder Swagelok cells were cycled to a specified potential or capacity. Cells were disassembled in an Ar glove box and the cathode powder was collected, washed with DMC, and dried under vacuum. For total scattering experiments, washed powders were loaded into 1.2 mm diameter kapton tubes sealed with epoxy at both ends. For XAS, powders were painted into homogeneous films on kapton tape. All *ex-situ* samples were prepared and transported under Ar.

First principles calculations

Structure prediction was performed using the *ab initio* random structure searching (AIRSS) method.[32] For a given system, AIRSS initially generates random structures, which are then relaxed to a local minima in the potential energy surface (PES) using density functional theory (DFT) forces. By generating large numbers of relaxed structures it is possible to widely cover the PES of the system. Based on general physical principles and system-

specific constraints, the search can be biased in a variety of sensible ways.[33] About 2200 Li–Fe–S structures were generated by AIRSS at stoichiometries of x = 0.5,1,1.5, 2, 3 and 4 in Li_xFeS_2.

AIRSS calculations were undertaken using the CASTEP DFT plane-wave code.[34] The gradient corrected Perdew Burke Ernzerhof (PBE) exchange-correlation functional[35] with spin-polarization was used in all calculations presented in this work. The core electrons were described using Vanderbilt "ultrasoft" pseudopotentials, the Brillouin zone was sampled using a Monkhorst-Pack grid[36] with a k-point spacing finer than $2\pi \times 0.07$ Å^{-1}. The plane wave basis set was truncated with a cut-off value of 350 eV.

The thermodynamical phase stability of a system was assessed by comparing the free energy of different phases. From the available DFT total energy of a given binary phase of elements *A* and *B*, $E\{A_aB_b\}$, it is possible to define a formation energy per atom as Equation 3:

$$E_f/\text{atom} = \frac{E\{A_aB_b\} - aE\{A\} - bE\{B\}}{a+b}. \tag{3}$$

The formation energies of each structure were then plotted as function of the *B* element concentration, $u = b/(a+b)$, starting at $u = 0$ and ending at $u = 1$. A convex hull was constructed between the chemical potentials at $(u, E_f/\text{atom}) = (0,0);(1,0)$ by drawing a tie line to join the lowest energy structures, which is valid provided it forms a convex function. This construction gives access to the 0 K stable structure, as the second law of thermodynamics demands that the (free) energy per atom is a convex function of the relative concentrations of the atoms.

Average voltages for the structures lying on the hull were calculated from the available DFT total energies. For two given phases on the hull, $A_{x_1}B$ and $A_{x_2}B$ with $x_2 > x_1$, the following two-phase reaction is assumed as Equation 4:

$$A_{x_1}B + (x_2 - x_1)A \rightarrow A_{x_2}B. \tag{4}$$

The voltage, *V*, is given by Equation 5,[37]

$$V = -\frac{\Delta G}{x_2 - x_1} \approx -\frac{\Delta E}{x_2 - x_1} = -\frac{E(A_{x_2}B) - E(A_{x_1}B)}{x_2 - x_1} + E(A), \quad (5)$$

where it is assumed that the Gibbs energy can be approximated by the internal energy, as the pV and thermal energy contributions are small.[37]

The low energy structures obtained by the AIRSS search were refined with higher accuracy using a k-points spacing finer than $2\pi \times 0.03\,\text{Å}^{-1}$ and an energy cut-off of 800 eV with more accurate pseudopotentials (see SI). The DFT+U approach implemented in CASTEP was used to correct self-interaction error in the GGA by adding the U parameter to the d orbital of the transition metal.[38] The U parameter can be chosen to assimilate any experimental band gap. U parameters ranging from 2 eV to over 5 eV have been reported for first principles calculations of various transition metal chalcogenides.[39–41] We have used a value of U_{eff} = 4 eV, as was used for Li−Fe−S−O compounds,[42] which falls within the range of reported U values.

X-ray absorption studies

Ex-situ XAS at the Fe K-edge was carried out at 20-BM-B at the Advanced Photon Source at Argonne National Laboratory for cells cycled at $C/40$, as described above. Spectra were collected in transmission mode. The data was calibrated to 7.112 keV,[43] and normalized by aligning the E_0 for each Fe foil to a reference spectra. Data was deglitched, normalized, and averaged using the open source program ATHENA.[44]

Operando pair distribution function studies

Operando total scattering experiments were carried out at 11-ID-B at the Advanced Photon Source at Argonne National Laboratory. A Perkin-Elmer amorphous Si-based area detector enabled rapid-acquisition of X-ray scattering measurements with an X-ray wavelength

of 0.2112 Å (≈58 keV). An AMPIX electrochemical cell[45] was assembled in an Ar-filled glove box with a free-standing pellet cathode composed of FeS_2:graphite/VulcanC (1:1 by weight):polytetrafluoroethylene (70:20:10 by weight). The free standing pellet cathode was about 160 μm thick and 13 mm in diameter. The electrolyte was 1 M $LiPF_6$ in EC:DMC in a 3:7 by volume, which soaked a GFD separator. Li metal served as both a reference and counter electrode. The cell was galvanostatically cycled with an applied current of 0.8722 mA and a C-rate of about $C/17$, based on the reaction of 1 mol FeS_2 with 4 mol Li in 17 h, and with potential limits of 1 V and 3 V. Due to time constraints of beamtime and our interest in characterizing later cycles in addition to the first discharge, *operando* studies were carried out at a faster rate than other cycling discussed here.

The background contribution of the *operando* cell was collected using an AMPIX cell assembled without the cathode. Experimental geometries were calibrated using CeO_2 powder and Fit2D freeware.[46] Fit2D was also used to integrate collected 2D data, which was acquired once every thirty minutes. From each set of integrated data, the real-space pair distribution function (PDF) was calculated by a Fourier transform using PDFgetX2,[47] with the structure factor taking into account the relative Li content based on a constant Fe:S ratio of 1:2 and with a $Q_{max} = 19$ Å^{-1}. PDFgui[48] was used to simulate PDFs and to fit data to published and calculated structures. Similar data collection and processing were carried out for *ex-situ* PDFs. Principal component analysis (PCA) was used to assess the local structure evolution during the first discharge. PCA was carried out using Origin Pro (OriginLab, Northampton, MA, USA), which yielded three significant principle components (PCs). Linear combinations were taken of the raw PCs such that there was a single component at the beginning of the reaction and a single component at the end of the reaction.[49] The weightings for these revised PCs were evaluated with a least squares linear combination analysis.

Results

Electrochemical cycling of FeS_2

For the first several cycles of FeS_2 unoptimized loose-powder Swagelok cells in carbonate electrolytes, we saw surprising reversibility and coulombic efficiency (Figure 2). The discharge-charge curves give clues about the mechanism(s) of Li storage. For example, there is ambiguity as to the presence of one or two plateaux in the first discharge [Figure 2(a)], which would suggest either one or two reactions occur. This has been addressed in previous literature and the mechanism (one *vs.* two reactions) appears to depend on the rate and/or temperature at which the cell is cycled.[19,27]

It is typical for the first discharge plateau of conversion materials to occur at lower potentials than in subsequent discharges.[2] The higher overpotential on the first discharge is ubiquitous and has been attributed to the extra energy associated with the creation of new interfaces of the many nano-scale domains formed during the first discharge.[4,5] There is also a contribution to the difference in potential of the first and subsequent discharges that arises from the difference in structure and composition of the first charge product from the initial material. For FeS_2 we saw a marked difference in both the potential and character of the first discharge compared to later cycling. During the first charge, there were two distinct plateaux separated by about 0.75 V. We observe a sloped region between the plateaux that contribute nearly one-third of the charge capacity. The features of the second discharge are more similar to those of the first charge than the first discharge. This is suggestive of a distinct reaction on the first discharge, which differs from subsequent cycles.

First principles calculations

About 2200 Li−Fe−S structures were generated by AIRSS for the reaction of FeS_2 with 1, 1.5, 2, 3 and 4 mol Li. While it is known that the discharge product resembles a com-

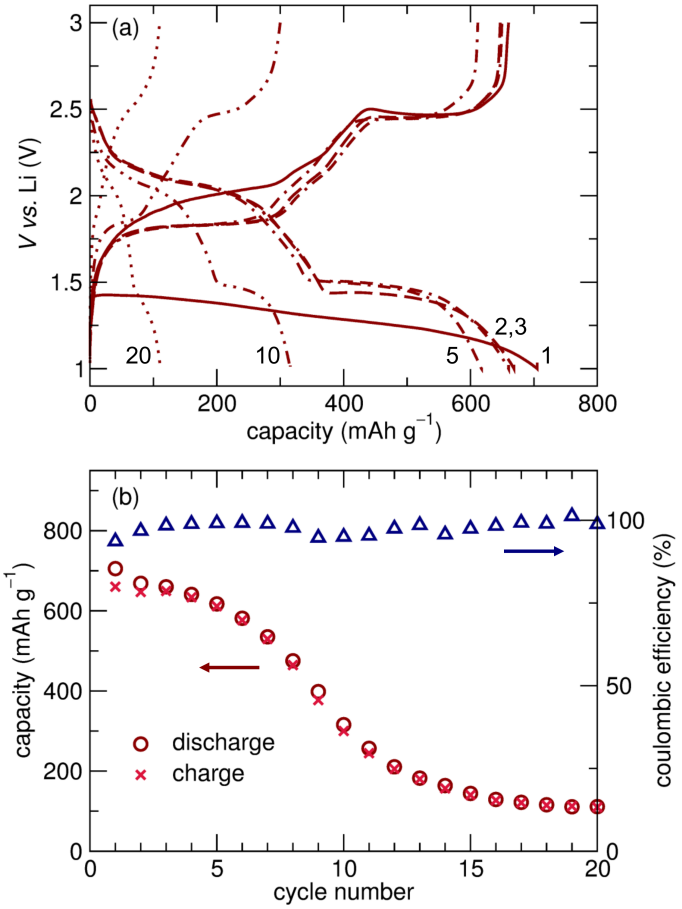

Figure 2: (a) Discharge-charge curves for FeS_2 at $C/40$ show good capacity retention for a conversion material over the first five cycles. Broken lines indicate later cycles, as numbered. (b) Capacity per cycle and coulombic efficiency show surprising reversibility for the first five cycles.

bination of Fe and Li_2S after reacting with 4 mol Li, treatment of multiple phases quickly becomes computationally expensive and so AIRSS calculations over the range were carried out to yield descriptions as single phase products. For the same reasons, the electrochemical curve is calculated based on the pseudobinary phase diagram (Figure 3).

The formation energies of calculated structures are plotted as a function of composition [Figure 3(a)]. Detailed information about the phases on the hull, and several just above it, are provided in Table 1.

Among the structures included in Table 1 are two previously published Li_2FeS_2 phases shown in Figure 1. We found the $P\bar{3}m1$ with octahedrally-coordinated Fe [Figure 1(b)] to be 0.110 eV/atom above the hull. For the $P\bar{3}m1$ structure with sites half occupied by Li and Fe tetrahedrally-coordinated by S [Figure 1(c)], two 1x2 supercells (provided in SI) were adapted with different patterning of Li and Fe on the sites, such that each is fully occupied by one or the other. These supercells were found to have formation energies about 0.050 eV/atom above the hull. While more rigorous methods would be needed to more exactly provide the relative energies of the these published phases to the hull, this would require computationally intensive efforts and have relatively low returns for this study. As such, we provide these formation energies to show that from a first pass, it is more likely that the MP or AIRSS phases, especially those in Table 2, are descriptive of the cycling products.

Tie lines connect the minimum energy structures and end members, FeS_2 and Li, to create the convex hull. The hull represents the thermodynamic equilibrium phases predicted to form as Li reacts with FeS_2 in the simplification of the ternary system to a pseudobinary. Assuming each phase transformation occurs as a two-phase reaction upon lithiation, a potential curve was calculated for the lowest energy structures [Figure 3(b)] using Equation 5.

We were not surprised to find differences between predicted and experimental potential curves for the first discharge. We expect the plateau of the experiment to have

a lower potential than was thermodynaically calculated due to the overpotential associated with kinetics of the reaction, especially the formation of many new surfaces during the nanostructuring that is well-documented for conversion materials.[4,5] Our experimental first discharge is at only a slightly lower potential than the calculated electrochemical curve [Figure 3(b)]. If treated as a true ternary, the combination of Fe and Li_2S would be energetically favorable to the predicted Li_4FeS_2. The predicted curve is not in agreement with second and later discharges either because, as will be discussed, the charge product is distinct from FeS_2 and so a different phase evolution occurs for the second and subsequent discharges.

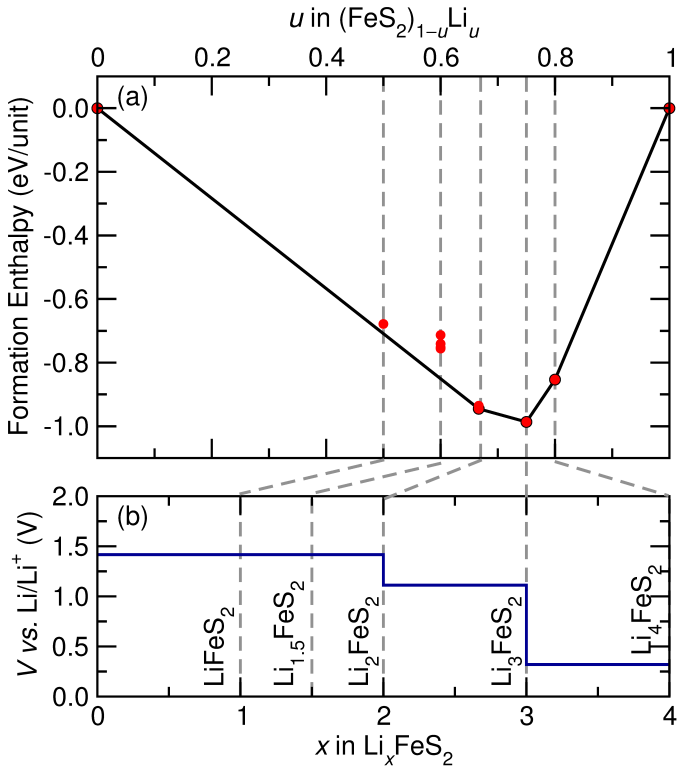

Figure 3: (a) Enthalpy per atom versus the fractional lithium concentration in the Li−FeS_2 system, simplifying the treatment of the system from a ternary to a pseudobinary. The convex hull is constructed by joining the stable structures obtained by the searches with tie lines. For further description of these phases, see Table 1. (b) Based on the stable phases, a prediction of the potential curve upon the first discharge involves several two-phase transformations: from FeS_2 to Li_2FeS_2, from Li_2FeS_2 to Li_3FeS_2, and finally from Li_3FeS_2 to Li_4FeS_2.

Since batteries do not necessarily operate under equilibrium conditions, we considered

Table 1: Description of the experimental and predicted Li_xFeS_2 phases. We indicate with a star ($\star$) the stable phases which are found on the convex hull. Descriptions of the structures obtained by AIRSS are presented in the Supporting Information.

Stoichiometry	x in Li_xFeS_2	Distance from the hull (eV/atom)	Space group	Structure origin	Structure motif
FeS_2 $\star$	0	0	$Pa\bar{3}$	ICSD[50]	Corner–shared octahedra
$LiFeS_2$	1	0.030	$P\bar{3}m1$	AIRSS	Edge–sharing octahedra
$Li_3Fe_2S_4$	1.5	0.095	$P2_1$	AIRSS	Edge–sharing tetrahedra
		0.097	$Pnma$	Derived from Materials Project ID:mp-768360[51] by relaxing the structure with zero magnetization	Edge–sharing tetrahedra
		0.103	$P\bar{1}$	AIRSS	Edge– and corner–sharing tetrahedra
		0.119	$Pnma$	Materials Project ID:mp-768360[51]	Edge–sharing tetrahedra
Li_2FeS_2 $\star$	2	0	$P2_1/c$	Materials Project ID:mp-775931[51]	Edge–sharing tetrahedra
		0.006	$P\bar{1}$	AIRSS	Edge– and corner–sharing tetrahedra
		0.045	$P3m1$	ICSD, model 1 adapted[22]	Layers of Li/Fe tetrahedra
		0.052	$P\bar{3}m1$	ICSD, model 2 adapted[22]	Layers of Li/Fe tetrahedra
		0.110	$P\bar{3}m1$	ICSD[17]	Layers of FeS_6 octahedra
Li_3FeS_2 $\star$	3	0	$P2_1$	AIRSS	Edge–sharing tetrahedra
Li_4FeS_2 $\star$	4	0	$P\bar{1}$	AIRSS	Fe–S zig-zag chains
Li $\star$		0	$Im\bar{3}m$	ICSD[52]	

several metastable phases near the hull. Despite variations of the relative stability, structures with similar structural motifs were near the hull for a range of Li content (1 to 2 mol Li). As such, we considered structures with Li:FeS_2 ratios of 1:1, 1.5:1 and 2:1 in comparing the local structure measured by PDF to predicted structures. FeS_2 did not achieve theoretical capacity during *operando* PDF studies, so for intermediate cycling products, we considered structures with corresponding Li content. We chose to focus on those of the stoichiometry $Li_3Fe_2S_4$ (also referred to in the text as $Li_{1.5}FeS_2$), previously described in Table 1. We also calculated the relative formation energies of selected structures at this composition when relaxed with DFT+U (Table 2).

Table 2: $Li_3Fe_2S_4$ structural formation energies, cell volumes and spin arrangements using GGA+U correction with $U_{eff} = 4$ eV.

Relative formation energy (meV/atom)	Symmetry	Volume (Å^3/f.u.)	Magnetic Ordering	Structure origin
0	$P2_1$	176.5	AFM	AIRSS
0.002	$Pnma$	178.2	FM	MP*
0.003	$P\bar{1}$	177.8	FM	AIRSS
0.015	$P2_1$	174.9	FM	AIRSS

* Derived from Materials Project ID:mp-768360[51]

The energetics of the system do not seem to change significantly after adding the U_{eff} parameter. However, an average increase of 15% in the cell volume is observed. The increment of the lattice parameters with increasing U_{eff} value has been observed in other studies.[38,53]

X-ray absorption studies

Ex-situ Fe K-edge XAS was carried out at various states of charge to probe the oxidation state and coordination of Fe during the cycling of the Li$-$$FeS_2$ electrochemical system. Samples were prepared by stopping cells at a particular capacity or potential during the cycling of loose-powder Swagelok cells at $C/40$ ($Q/10$). For complex and non-equilibrium systems, such as conversion materials, *in-situ* and *operando* experiments are ideal for the

most representative data. However, we compared *operando* and *ex-situ* PDF for similar states of charge and saw good agreement between features of each (Figure S1), which gave us confidence in the *ex-situ* XAS. For both *ex-situ* PDF and XAS, samples were prepared just prior to experiments to minimize changes of the material between cycling and measurements. Due to extreme disorder in these materials after cycling, we focus on the near-edge energy range of the XAS data, rather than attempting to carry out an analysis of the fine structure. The discharge-charge curves for the first 1.5 cycles are shown in Figure 4(a) and are marked at each point a cell was stopped for an *ex-situ* measurement. The first discharge differs slightly from that shown in Figure 2(a), which is due to cell-to-cell variation from the non-optimized loose-powder cells employed. In this cell, a slight increase in potential can be seen at about 2 mol Li; this could arise from the change in the particle size upon lithiation, as the bulk particles are broken into smaller domains.[7,54] The XAS measured at each state of charge, and of FeS_2 as a reference, are shown for each half cycle [Figure 4(b), (c), and (d)].

During the first discharge, we observed a slight change of slope with the reduction of Fe^{2+} in FeS_2. The product of the first discharge differed from bulk Fe [Figure S2(a)], which is in part due to the incomplete reaction of FeS_2 over the first discharge. The nature of the XAS of the discharge product was also impacted by the small domain size and disorder of Fe clusters that formed with discharge. This has been observed for FeS_2 by XAS previously and will be discussed in more detail in the PDF analysis and discussion sections.

The character of the post-edge, above 7.12 keV, changes from the pristine material with reduction halfway through and at the end of the first discharge [Figure 4(b)]. Over the first charge, the slope of the edge increases with oxidation. Also, a more well-defined, sharper pre-edge peak emerges upon charging to 1.9 V [Figure 4(c)], just beyond the lower potential plateau [Figure 4(a)]. This pre-edge peak grew during the rest of the charge process, over which there were relatively minor changes to the edge and post-edge features [Figure 4(c)]. The evolution of the post-edge during the slope and high potential plateau

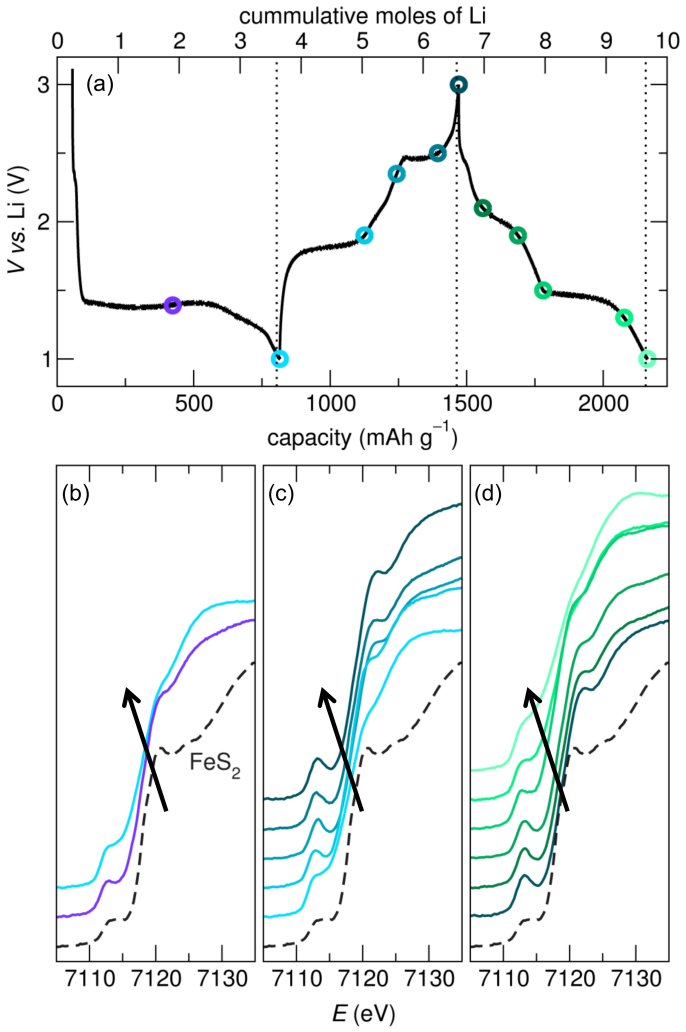

Figure 4: (a) Representative 1.5 cycles of galvanostatic cycling at $C/40$ marked at each potential or capacity at which a cell was stopped for *ex-situ* XAS. (b) The corresponding XAS for the first discharge, (c) the first charge, and (d) the second discharge. FeS_2 is plotted in each panel for reference.

of the electrochemistry could correspond to slight changes in the local coordination of Fe, for example, bond distances and bond angles.

The evolution of the XAS over the second discharge was quite different than that observed for the first discharge. Over the high potential plateau and the sloped region (above 1.5 V), the edge remained quite similar and the post-edge evolved slightly [Figure 4(a) and (d)]. Over the lower potential plateau, the XAS saw a more pronounced change suggestive of the reduction of Fe [Figure 4(a) and (d)]. The second discharge product, similar to that of the first discharge, differed from bulk Fe [Figure S3(a)], likely due to small domain sizes of Fe. At these cycling conditions, there is ambiguity as to whether an intermediate phase forms on the first discharge. It has been previously reported to vary with electrolyte, temperature, rate, and particle size.[19,26,27] The XAS of the first and second discharge products were similar and resembled small clusters of metallic Fe and, possibly, remaining FeS_2 or a ternary structure [Figure S2(a)].[55] Differences between the spectra of the discharge products and the bulk Fe reference are likely a consequence of small clusters of Fe and local disorder,[26] which we also see evidence of by *operando* PDF.

The difference of XAS evolution over the lower and higher potential plateaux of the cycling was revealing about the mechanisms at play. There was a clear conversion over the lower plateau, but relatively minor changes in the XAS at higher potentials, suggesting a different mechanism of Li reaction in this potential range, one with minimal changes to the local environment of Fe. The similarity of the XAS at higher potentials suggests the products are structurally similar. In previous work, Totir *et al.* interpreted the similarity of the Fe K-edge to mean that S redox was predominant at higher potentials.[24] However, a follow-up study using S K-edge XAS did not see clear evidence for oxidation of S to disulfide.[30] These studies led Totir *et al.* to believe that the charge product consisted of pyrrhotite (of the form Fe_xS_y) and S,[30] as had been proposed by other work.[28] We find the XAS of the charge product to be distinct from that of Fe_7S_8 [Figure S2(a)]. In particular, the pre-edge character of XAS above the lower plateau is suggestive of tetrahedrally-

coordinated Fe,[56] similar to that of a cubanite ($CuFe_2S_3$, $F\bar{4}3m$)[57] standard [Figure S2(b)], in which Cu and Fe share tetrahedrally-coordinated sites and Fe has an average 2.5+ oxidation state. Previous XAS studies of FeS_2 that did not see a pre-edge peak were carried out using ether-based electrolytes, in which the electrochemical behavior of S will vary.[27]

Operando pair distribution function studies

Operando PDF of a cycling Li$-$$FeS_2$ cell was collected over the first 4.5 cycles (Figure S3). On the first discharge, FeS_2 reacted with Li over a single, sloping plateau near 1.5 V, yielding a capacity of 2.6 mol Li [Figure 5(a)]. This differs slightly from slower cycling in which it was unclear if one or two plateaux were present on the first discharge [Figure 2(a)]. The general behavior and features of the discharge-charge curves of the *operando* cell were similar to those seen in the cycling of loose-powder Swagelok cells.

Over the first discharge, *operando* PDF shows a change in local structure from FeS_2 to Fe- and Li_2S-like domains [Figure 5(b)]. PCA was carried out to discern if intermediate local structures evolved during the first discharge. By PCA and linear combination transformations to satisfy criteria, as described by Chapman *et al.*,[49] we determined three significant PCs. The first PC is FeS_2 and matches the pattern before cycling [Figure 5(b)(i)]. The second PC is representative of the product of the first discharge, which resembles Fe and Li_2S [Figure 5(b)(ii)]. The third PC forms intermediately and is then consumed. This third PC does not resemble the ternary local structures observed in later cycles, but does have some features in common with the product of the fifth discharge. The PCs and the percentages in which they appear over the first discharge can be found in Figure S4 and Figure S5, respectively. For the discharge product, the intensity of peaks at even 14 Å was low, indicating poor long-range order, as is expected for conversion materials.[4,5] Further analysis of the discharge product will be discussed in following sections.

The first charge took place over two plateaux and a sloped region between them and achieved a charge capacity of about 2.3 mol Li (Figure 6). The first plateau [Figure 6(a)(ii)

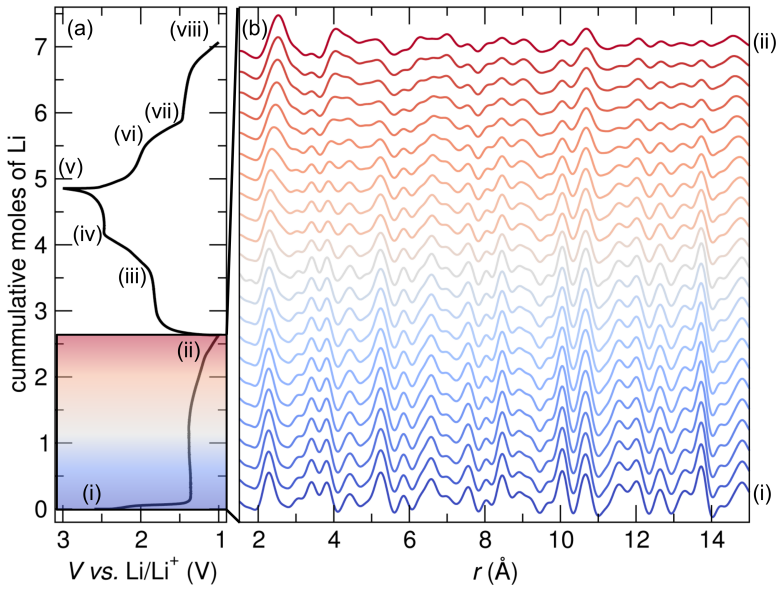

Figure 5: (a) The first 1.5 cycles of *operando* electrochemistry at $\approx C/17$. (b) The corresponding PDFs for the first discharge show conversion of (i) FeS_2 to (ii) Fe- and Li_2S-like products. The PDF also shows a decrease in crystallinity with cycling by the decreased intensity of peaks beyond 6 Å.

to (iii)], near 1.9 V, contributed 1 mol Li to the capacity and the second [Figure 6(a)(iv) to (v)], at about 2.5 V, contributed 0.7 mol Li. Between them, the sloped region [Figure 6(a)(iii) to (iv)] contributed a non-negligible 0.6 mol Li. Over the first charge, there was a conversion from the Fe- and Li_2S-like domains [Figure 6(c)(ii)] to another local structure [Figure 6(c)(v)] distinct from both FeS_2 [Figure 6(b)(i)] and the first discharge product [Figure 6(b)(ii)]. Above the lower plateau [Figure 6(a)(iii) to (v)], the first three major peaks between 1.5 Å and 5 Å, shifted to lower *r*. As was observed for the first discharge product, the higher *r* peaks decreased in intensity, indicating a decrease in long-range order.

We found electrochemical features during the second discharge similar to those of the first charge, with plateaux near 2 V [Figure 7(a)(v) to (vi)] and 1.5 V [Figure 7(a)(vii) to (viii)] and a total discharge capacity of about 2.2 mol Li. During the second discharge, the local structure initially evolved with the shifting of low and moderate *r* peaks to higher *r* [Figure 7(b)(v) to (vii)], followed by a change of the local structure to resemble the first

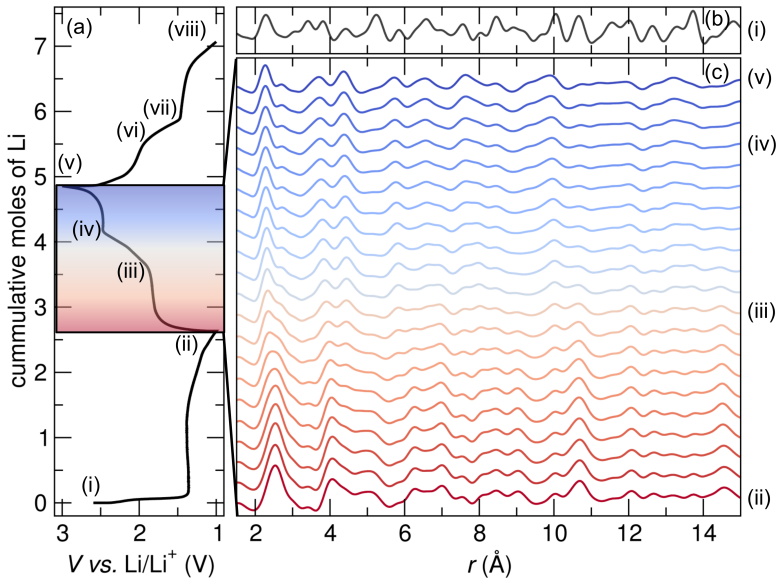

Figure 6: (a) First 1.5 cycles of *operando* electrochemistry at $\approx C/17$. (b) PDF of the FeS_2 before cycling. (c) The PDFs for the first charge show conversion of (ii) discharge products (Fe- and Li_2S-like domains) to (iii) an intermediate phase and then [(iii) to (iv)] the shifting of pairwise interactions to lower r over the sloped region and (iv) the high potential plateau with continued charging. The local structure shows that [(c)(v)] the charge product has much less long-range order and is not FeS_2 [(b)(i)].

discharge product [Figure 7(b)(vii) to (viii)].

Considering the first 1.5 cycles of *operando* PDF together, a few key observations can be made. Similar to XAS, PDF showed that the discharge products locally resembled Fe and Li_2S [Figure 5(b)(ii) and Figure 7(b)(viii)] and that FeS_2 [Figure 5(b)(i)] was not recovered on charge[Figure 6(b)(v)]. The shifting of peaks during the first charge and second discharge (as well as during subsequent cycles) suggests the charge product is structurally similar to an intermediate. This is in line with the minor changes of the post-edge of XAS in this regime of potential and Li content. In the high potential regime of the second discharge, we propose there is some storage of Li by a host structure by an insertion-extraction mechanism at lower Li content, followed by conversion to Fe- and Li_2S-like domains at higher Li content and lower potentials. Further analysis of discharge, charge, and intermediate products are discussed in greater detail following.

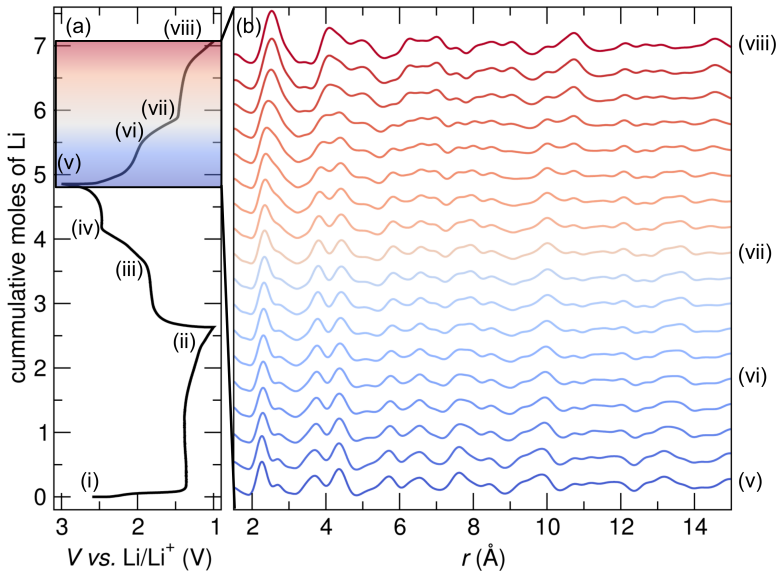

Figure 7: (a) First 1.5 cycles of *operando* electrochemistry at $\approx C/17$. (b) The corresponding PDFs for the second discharge suggest a similar mechanism as the first charge, which is distinct from the first discharge. [(v) to (vi)] Over the high potential plateau and [(vi) to (vii)] the sloped region, there is an increase in the pairwise interaction lengths with reduction, an expansion of the local structure, suggestive of Li insertion into a host structure. [(vii) to (viii)] Over the low potential plateau, at about 1.5 V, there is a conversion to (viii) Fe- and Li_2S-like products, similar to [Figure 5(b)(ii)] the products of the first discharge.

Pair distribution function analysis of intermediate ternary products

Several structures have been proposed to form during the cycling of FeS_2. Among those are phases hypothesized to accommodate a range of Li content and, accordingly, store charge by a Li insertion-extraction mechanism at high potentials and low Li content. We also see evidence for this mechanism in our study. By the analysis of *operando* PDF, we elucidate new information about the local structure of the ternary intermediate and a related charge product.

Among the calculated and published ternary Li−Fe−S phases we considered, there were a number of local structural motifs present. At the smallest correlation distance, we saw a difference of Fe octahedrally- or tetrahedrally-coordinated by S in the simulated PDF. Fits to intermediate cycling products (collected at 1.56 V and 1.3 mol Li, along the sloped region of the second discharge) show that published Li_2FeS_2 with FeS_6 octahedra[17] does

not capture the features of the measured PDF as well as structures with FeS_4 tetrahedra (Figure S6). This is consistent with the pre-edge peak in XAS at these potentials, which is indicative of tetrahedrally-coordinated Fe (Figure 4).

To analyze the PDF of the intermediate and related charge products of cycling, we focused on PDF measured over the sloped region of the second discharge at 1.74 V with about 1.2 mol Li. Since the full capacity was not achieved and calculated structures at various compositions had similar local motifs, we considered several metastable calculated phases at the composition $Li_{1.5}FeS_2$ with FeS_4 tetrahedra (Figure 8). The metastable $Li_{1.5}FeS_2$ structures considered generally consist of Li between 1D or quasi-1D chains of FeS_4 tetrahedra, each with a unique local motif beyond the first coordination shell. The $P\bar{1}$ structure [Figure 8(a)] consists of disrupted corrugated chains, which meet to form a group of four corner-sharing tetrahedra, referred to hereafter as a "tetrad" motif [Figure 9(i)] (GGA+U structure used, see Table 2). The $P2_1$ structure [Figure 8(b)] has edge-sharing FeS_4 tetrahedra that arrange as corrugated chains [Figure 9(ii)], with Li between them (by PBE, see Table 2). The $Pnma$ phase [Figure 8(c)] has linear chains of edge-sharing FeS_4 tetrahedra [Figure 9(iii)] (derived from Materials Project,[51] relaxed by PBE, see Table 2). Among the other calculated structures with tetrahedrally-coordinated Fe, each had one of these three motifs.

We fit the three representative structures shown in Figure 8 to an intermediate product along the slope of the second discharge at 1.74 V and 1.2 mol Li. The data was fit between 1.5 Å and 5.5 Å and lattice parameters, non-special angles, a correlated motion parameter (`delta1` in PDFgui), and the U_{iso} of each atom were refined in a single-phase fit with a nanoparticle size (the parameter `spdiameter` in PDFgui) of 40 Å. It is important to note that the "tetrad" phase has the more complex local structure and the lowest symmetry; this enables refinement of more Fe−Fe correlation distances and parameters that contribute to the goodness of fit of this local motif to measured PDF.

Fitting over this small range, on the same length scale of the structural motifs, gave

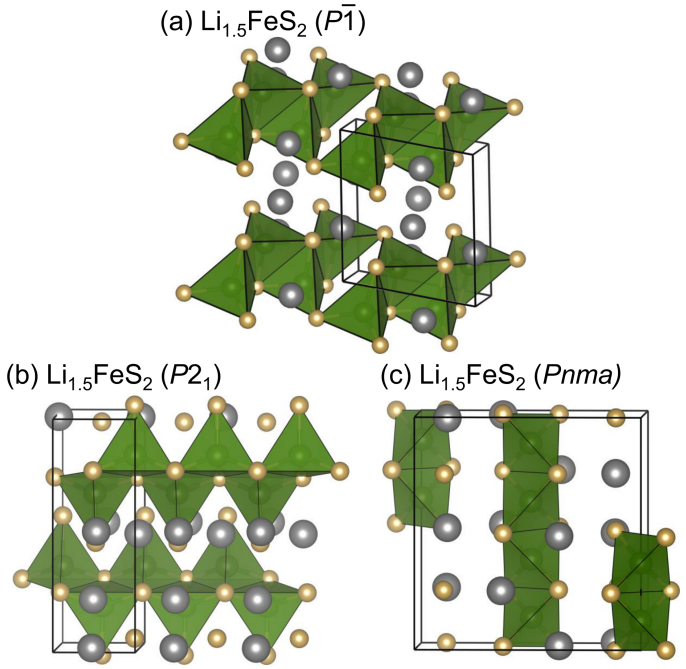

Figure 8: Several structures with the composition $Li_{1.5}FeS_2$ with tetrahedrally-coordinated Fe from AIRSS calculations. (a) $Li_{1.5}FeS_2$ with $P\bar{1}$ symmetry has both edge- and corner-sharing FeS_4 tetrahedra (GGA+U). (b) $Li_{1.5}FeS_2$ with $P2_1$ symmetry has corrugated chains of edge-sharing tetrahedra (PBE), and (c) $Li_{1.5}FeS_2$ with $Pnma$ symmetry has linear chains of edge-sharing tetrahedra (derived from Materials Project, relaxed by PBE).

good fits with small difference curves (Figure 9). While the corrugated and linear chains [Figure 9(ii) and (iii)] fit the local structure quite well [Figure 9(b) and (c)], there are still several correlations not completely captured by these motifs. Both the fit and the nature of the difference curve show the tetrad structural motif (in the $P\bar{1}$ phase) best models the local structure of the measured PDF [Figure 9(i) and (a)]. The low symmetry of the $P\bar{1}$ structure and the corresponding larger number of refined parameters undoubtedly contribute to the goodness of fit to the measured data. This structure also has the most variety of connectivity, with both edge- and corner-sharing tetrahedra, which enables it to fit the local structure. When refined to higher *r*, the overall quality of fit decreases, which suggests the local and average structures are different. In particular, it appears that the local structure resembles the local motifs described by the calculated phases, but there is insufficient correlation of these units to give a periodic structure. We carried out fits to the three published structures (shown in Figure 1 and described above) with similar fitting conditions as the calculated structures and less satisfactory fits (Figure S7).

Of the local structures considered, the tetrad motif present in the $Li_{1.5}FeS_2$ with $P\bar{1}$ symmetry gave the best local fit. Accordingly, this is a possible structural unit in the intermediate products. However, there could be a variety of local motifs contributing to the measured PDF. From PDF and XAS, we know the local structure of the intermediate and charge products are similar. By fitting the $P\bar{1}$ structure to 15 Å at various states of charge above the lower potential plateau, on both the first charge and second discharge, we see many of the features are captured (Figure S8 and Figure S9). It is important to note that the average structure is not well-defined by the $P\bar{1}$, or any other, of the phases we considered; when we extend the good local fit for the tetrad motif to even 15 Å, the overall fit is not as good (Figure S8).

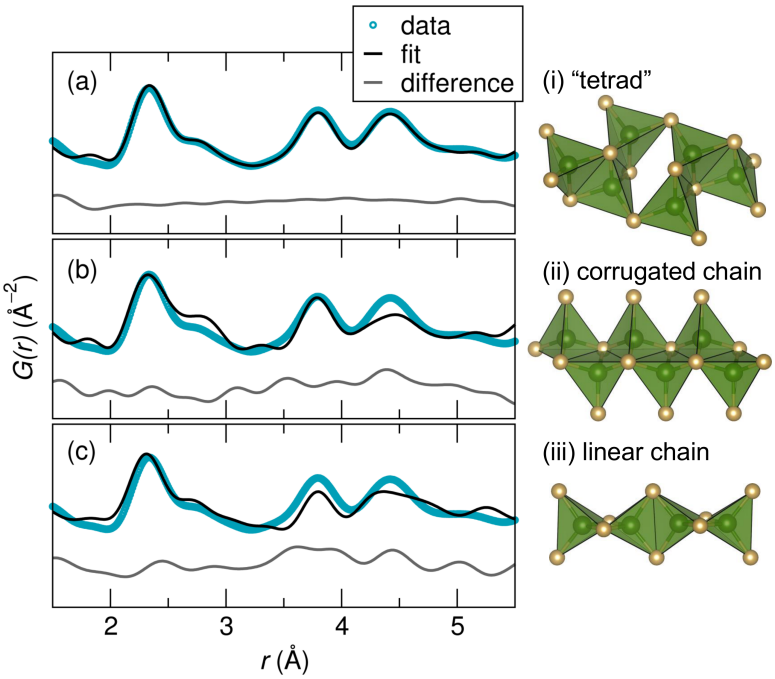

Figure 9: Fits of three calculated structures with the composition $Li_{1.5}FeS_2$ with tetrahedrally-coordinated Fe to data collected at 1.74 V and 1.2 mol Li during the second discharge and various local structure motifs. (a) $Li_{1.5}FeS_2$ with $P\bar{1}$ symmetry has both edge- and corner-sharing FeS_4 tetrahedra, which we refer to as (i) a "tetrad". (b) $Li_{1.5}FeS_2$ with $P2_1$ symmetry has (ii) corrugated chains of edge-sharing tetrahedra. (c) $Li_{1.5}FeS_2$ with $Pnma$ symmetry has (iii) linear chains of edge-sharing tetrahedra.

Pair distribution function analysis of discharge products

By XAS,[24,25,54] transmission electron microscopy,[4,5,58] and [26]Fe Mössbauer,[26] among other methods, researchers have previously found that the metal formed during the discharge of conversion electrodes tends to occur as disordered clusters of metal atoms on the order of 10 Å to 50 Å in diameter. Deviations of the structure of nanoparticles from the bulk structure has been observed for several systems, including gold nanoparticles.[59]

As previously mentioned, for FeS_2 the first and second discharge products locally resembled Fe and Li_2S. Upon a closer look we found equilibrium body-centered cubic (*bcc*) Fe did not fully capture the local structure of the first discharge product (Figure S10), which has been previously observed for other Fe-based conversion electrode materials.[11,13] Comparing the PDF of the first discharge product to a two-phase fit of Li_2S and *bcc* Fe, *bcc* Fe contributes an extra peak at 5.6 Å and does not capture the peaks at 6.3 Å and 8.7 Å (Figure S10). From similar comparisons to the local structure of face-centered cubic and body-centered tetragonal Fe, we found these local structures were not a good match to the measured PDF. We also compared the local structure of the first discharge to hexagonal close-packed (*hcp*) Fe, which was close, but like *bcc* Fe had extra or missing peaks (Figure S10); *hcp* Fe captured the peaks at 6.3 Å and 8.7 Å that *bcc* Fe was missing, but had extra features at 3.6 Å and 5.6 Å.

To better model the local structure, we employed a supercell of *bcc* Fe whose atomic positions were perturbed from their ideal sites, using the RMCProfile software suite.[60] A $3\times3\times3$ supercell of 54 atoms was generated from a single unit cell of $Im\bar{3}m$ (*bcc*) Fe with Fe in the *2a* Wyckoff site at $(0, 0, 0)$. Atoms were allowed to translate a maximum of 0.01 Å per move and a minimum approach distance of 2.46 Å was applied, employing approximately 5×10^6 Monte Carlo moves. The relaxation yielded a local structure that offered a good compromise between *bcc* and *hcp* Fe (Figure S10). The structure produced by the simulation was then used in a two phase fit of the discharge product with Li_2S as the second phase. In combination with Li_2S, the disordered Fe, with an approximate cluster

diameter of 10 Å to 12 Å (set as `spdiameter` in PDFgui[48]), captures the dominant features of the first discharge product in the range of 1.5 Å to 15 Å [Figure 10(a)]. We know from previous work that the diameter of a particle or cluster will relate to the damping of the signal from that material in the PDF.[59] For these fits, the lattice parameters and U_{iso} of all atoms were refined. Visualization of the initial *bcc* Fe supercell and the disordered Fe structures are available in Figure S11.

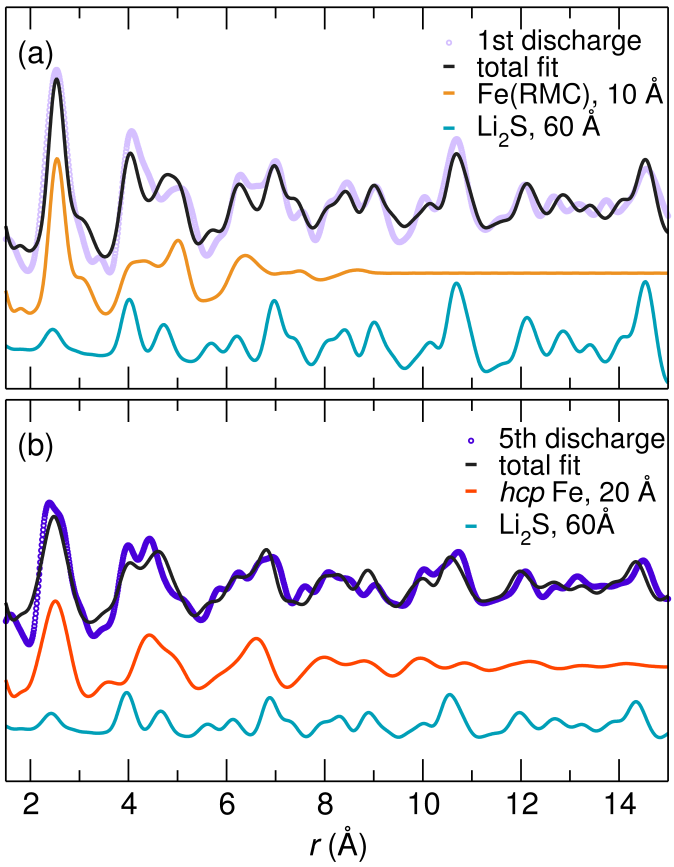

Figure 10: (a) Two-phase fit of the first discharge and contributions from each phase: disordered Fe from the relaxation of a *bcc* Fe supercell with a particle diameter of 10 Å and Li_2S with a particle diameter of 60 Å. (b) Two-phase fit of the fifth discharge and contributions from each phase: *hcp* Fe with a particle diameter of 20 Å and Li_2S with a particle diameter of 60 Å.

The local structure of the first, second, and third discharge products were similar [Figure 11(a)], and can therefore be described by clusters of disordered Fe and Li_2S. The PDF of the fourth and fifth discharge products were different than the previous and better de-

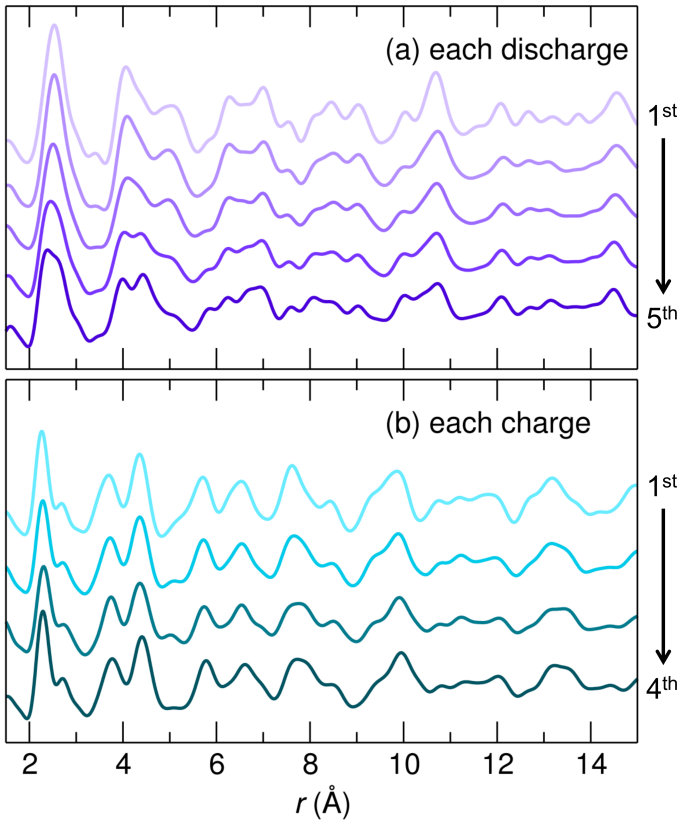

Figure 11: (a) PDFs of the first through fifth discharges of FeS_2 show changes in the local structure with cycling. The first through the third discharge products are similar, corresponding to clusters of disordered Fe and Li_2S locally. The fourth and fifth discharge products have a different local structure, better matched to small clusters of *hcp* Fe and Li_2S. The fits of the first and fifth discharge products can be found in Figure 10. (b) PDFs of the first through fourth charge products show similar local structures.

scribed as a combination of *hcp* Fe and Li_2S. A two-phase fit of the fifth discharge product with about 20 Å diameter clusters of *hcp* Fe and Li_2S model the local structure well [Figure 10(b)]. This analysis of the discharge products does not preclude other species that may be present in small amounts.

It appears that Fe clusters grow with subsequent discharges, possibly as the crystallinity of the system decreases with each cycle, which could enable increased Fe diffusion. Despite the evolution of the discharge product with cycling, there are only minor changes to the charge product [Figure 11(a)]. Despite the apparent growth of clusters and their resemblance to *hcp* Fe at discharge in later cycles, the cluster formation appears to be mostly reversible, as no major changes are evident in the four charge products over which PDF was collected [Figure 11(b)].

Discussion

By a combination of first principles calculations, *operando* PDF, and *ex-situ* XAS, we bring new insight to the local structure evolution at the cathode in Li$-$$FeS_2$ cells. We make a point of examining later cycles in addition to the first discharge to understand the processes most representative of the system. In the cycling of micron-sized particles of FeS_2 at room temperature at $C/17$ in carbonate electrolyte, we observed conversion to Fe- and Li_2S-like domains during the first discharge by *operando* PDF. On the first charge we observed a conversion from Fe and Li_2S to an intermediate, ternary local structure over the lower potential plateau. With continued oxidation, the low *r* peaks shift, rather than forming a new local structure. The shift of these peaks with oxidation and reduction corresponds to the expansion and contraction of bond lengths and, consequently, cell parameters with cycling, suggestive of a Li insertion-extraction mechanism (similar to the intercalation of Li for $Li_{1-x}CoO_2$) above the lower potential plateau between the ternary intermediate and a related charge product. *Ex-situ* Fe *K*-edge XAS also shows only minor changes above

the lower potential plateau. An insertion-extraction regime has been proposed in previous reports and our *operando* PDF enables visualization of this mechanism.

The combination of *operando* PDF and *ex-situ* XAS also allows us to expand upon hypothesized phases to describe the intermediate, ternary local structure and the related charge product. The pre-edge feature in Fe *K*-edge XAS and the first correlation peak in PDF indicate an intermediate product with tetrahedrally-coordinated Fe. The tetrahedral features persist in both the PDF and XAS for all electrochemistry above the lower potential plateau. The combination of this data is in contrast to previous literature that suggests octahedral coordination of Fe by S, either in ternary phases or in off-stoichiometry Fe_xS_y pyrrhotite.[27,28,30] However, pyrrhotite has primarily been reported for ether-based electrolytes, in which S electrochemistry and solubility are known to differ and could impact the structural evolution. For our study in a carbonate-based electrolyte solution, we see a poor fit of phases with FeS_6 octahedra to our data (Figure S6).

There are previously proposed ternary phases with FeS_4 tetrahedra [Figure 1(c) and (d)], however, we found the local structure of these phases beyond the first coordination shell were not a good fit to measured PDF (Figure S7).[22,23] To further explore the local structure, AIRSS was employed to predict a library of ternary structures with various local motifs. We found reasonably good fits for those motifs with linear or corrugated chains of edge-sharing FeS_4 tetrahedra at intermediate states of charge. The best local fit, however, was for a "tetrad" motif, which has both edge- and corner-sharing FeS_4 tetrahedra. All three motifs capture most of the local features of the intermediate PDF well, but none have great agreement to the average structure, indicating there is poor correlation at higher *r*. It is well-known that conversion systems lack long-range order, making our findings consistent with previous reports on conversion systems.[5–7]

The collection and analysis of PDF over 4.5 cycles allows a unique opportunity to relate structure and performance. We see over the five discharge products an increase in the size of Fe clusters, modeled in fits as `spdiameter`. As the clusters grow, there is also a

change from disordered Fe to a local structure resembling *hcp* Fe. The larger diameter could enable the lower energy, more ordered Fe structure. Previous studies suggest that Fe-based conversion systems show favorable reversibility relative to Cu-based analogues due in part to the smaller size of Fe particles formed, with the cluster size limited by the diffusivity of the metal during discharge.[5] The combination of small angle X-ray scattering and PDF has been previously employed by Wiaderek *et al.* to reveal a dependence of cluster size on anion chemistry for Fe-based conversion electrodes, with fluorides forming larger particles than oxides (35 Å compared to 20 Å).[13] For FeS_2, we find Fe clusters for the first discharge on the order of 10 Å in diameter. Combining the results of the study by Wiaderek *et al.* with this one,[13] it is possible that nanoparticle size varies with anion electronegativity. However, it is unclear if this trend is exclusively applicable to Fe-based materials or is more general. Other factors, such as the degree of ionicity or covalency of bonds, could be at play in the impact of anion chemistry on metal cluster size. Despite the evolution in the discharge products, the first four charge products remain quite similar, even as the charge capacity fades slightly. *Operando* PDF at later cycles could further inform failure mechanisms for this system.

The intriguing difference between FeS_2 and a number of other conversion systems is the dual modes of storage. FeF_2,[4] MnO,[7] CuF_2,[8] and many others store Li by a single conversion step. In isostructural pyrite CoS_2, which does have multiple reactions, the observed intermediate products are a combination of Li_2S and Co−S binaries.[61] We present here strong evidence that the cathode of an Li−FeS_2 cell operates by two different mechanisms beyond the first discharge under cycling conditions similar to those employed here. At slower rates or higher temperature, the first discharge can involve an intermediate product, but this would be two conversion steps, rather than the pairing of insertion-extraction and conversion reactions. The combination of insertion-extraction and conversion seen in the second and subsequent cycles of FeS_2 system are similar to observations for VS_4, which on charge undergoes conversion from V clusters and Li_2S to a ternary $Li_{3+x}VS_4$ structure

that is stable over a range of Li content, and so then undergoes an insertion-extraction mechanism from the host structure at higher potentials.[9] The reversible behavior of FeS_2 could arise from the two types of charge storage mechanisms that occur.

Conclusions

This examination of the Li−FeS_2 secondary energy storage system provides new insights into the previously studied cycling mechanism at slow rates, room temperature, and in a carbonate-based electrolyte by *operando* PDF and *ex-situ K*-edge XAS. During the first discharge, FeS_2 undergoes conversion to Fe- and Li_2S-like domains under these cycling conditions. Initially, the Fe clusters are disordered, not quite resembling *bcc* or *hcp* Fe. In continued cycling, the Fe clusters grow and the local structure more closely resembles *hcp* Fe, possibly stabilized by the growth of metal clusters.

The first charge product is not FeS_2, and consequently, the second discharge follows a different evolution of local structure than the first. The first charge occurs as two steps: (i) conversion between Fe- and Li_2S and a ternary intermediate over the lower plateau and (ii) an insertion-extraction reaction with a host structure over the higher potential slope and plateau. The Li insertion-extraction is evidenced in the PDF by the shifting of low *r* peaks in real space, corresponding to expansion/contraction of the structure as bond lengths increase/decrease with reduction/oxidation. The related intermediate and charge products have tetrahedrally-coordinated Fe. We suggest several structures with local motifs that capture the low *r* features of the measured PDF well and describe the local structure of the intermediate cycling products. The second discharge appears to follow the same steps as the first charge in the reverse order. We hypothesize that the hybrid modes of storage - insertion/extraction and conversion - could be important in identifying promising candidates for next-generation, high capacity electrode materials.

In addition to our contribution to the understanding of FeS_2 as a conversion electrode,

we also show effective methodology for investigating dynamic and disordered systems, including conversion reaction electrode candidates. We especially highlight the utility of combined computational and local structure methods. Further, we show that the application of *operando* methods and structural characterization well beyond the first discharge reveal useful insight into the mechanisms of charge storage and even cell failure. This work also contributes to the literature on conversion electrodes by characterizing the mechanisms of a relatively reversible system. Mechanistic studies with advanced characterization methods permit the identification of general rules for more reversible candidates, toward realizing the promise of conversion reaction systems for electrochemical energy storage.

Acknowledgments

M.M.B. acknowledges support by the Fletcher Jones and Peter J. Frenkel Foundation Fellowships. V.V.T.D.N. is supported by the University of California President's Postdoctoral Fellowship and the UCSB Canifornia NanoSystems Institute Elings Prize Fellowship. V.V.T.D.N. gratefully acknowledges the Southern California Electrochemical Energy Storage Alliance (SCEESA), supported by the UCSB CNSI. Experiments at UCSB made use of MRL facilities, supported by the MRSEC Program of the NSF under Grant No. NSF-DMR 1121053. M.A.L. was supported by the RISE program through NSF-DMR 1121053. This work was partially supported by the IMI Program of the National Science Foundation under Award No. DMR 08-43934. M.M. and A.J.M. acknowledge the support from the Winton Programme for the Physics of Sustainability. C.P.G. and S.B. thank EPSRC for financial support. This research made use of resources of the Advanced Photon Source, a U.S. Department of Energy (DOE) Office of Science User Facility operated for the DOE Office of Science by Argonne National Laboratory under Contract No. DE-AC02-06CH11357. X-ray absorption experiments were performed at APS 20-BM-B under GUP-41555. Sector 20 operations are supported by the US DOE and the Canadian Light Source. X-ray scatter-

ing experiments were performed at APS 11-ID-B under GUP-42128 and GUP-45245. The authors also thank Professor Anton Van der Ven for helpful discussions.

Associated Content

The Supporting Information is available free of charge through the ACS Publications website.

Further cycling of *operando* PDF, a comparison of *operando* and *ex-situ* PDF at similar states of charge, Fe *K*-edge XAS of several standards, additional fits of measured PDF to published phases and with higher *r* refinements, and descriptions of calculated structures.

References

(1) Goodenough, J. B.; Kim, Y. Challenges for Rechargeable Li Batteries. *Chem. Mater.* **2009**, *22*, 587–603.

(2) Cabana, J.; Monconduit, L.; Larcher, D.; Palacín, M. R. Beyond Intercalation-Based Li-Ion Batteries: The State of the Art and Challenges of Electrode Materials Reacting Through Conversion Reactions. *Adv. Energy Mater.* **2002**, *22*, E170–E192.

(3) Hayner, C. M.; Zhao, X.; Kung, H. H. Materials for Rechargeable Lithium-Ion Batteries. *Annu. Rev. Chem. Biomol. Eng.* **2012**, *3*, 445–471.

(4) Wang, F. et al. Conversion Reaction Mechanisms in Lithium Ion Batteries: Study of the Binary Metal Fluoride Electrodes. *J. Am. Chem. Soc.* **2011**, *133*, 18828–18836.

(5) Wang, F.; Yu, H.-C.; Van der Ven, A.; Thornton, K.; Pereira, N.; Zhu, Y.; Amatucci, G. G.; Graetz, J. Ionic and Electronic Transport in Metal Fluoride Conversion Electrodes. *ECS Trans.* **2012**, *50*, 19–25.

(6) Lowe, M. A.; Gao, J.; Abruña, H. D. In Operando X-ray Studies of the Conversion Reaction in Mn_3O_4 Lithium Battery Anodes. *J. Mater. Chem. A* **2013**, *1*, 2094–2103.

(7) Butala, M. M.; Danks, K. R.; Lumley, M. A.; Zhou, S.; Melot, B. C.; Seshadri, R. MnO Conversion in Li-ion Batteries: In situ Studies and the Role of Mesostructuring. *ACS Appl. Mater. Interfaces* **2016**, *8*, 6496–6503.

(8) Hua, X.; Robert, R.; Du, L.-S.; Wiaderek, K. M.; Leskes, M.; Chapman, K. W.; Chupas, P. J.; Grey, C. P. Comprehensive Study of the CuF_2 Conversion Reaction Mechanism in a Lithium Ion Battery. *J. Phys. Chem. C* **2014**, *118*, 15169–15184.

(9) Britto, S.; Leskes, M.; Hua, X.; Hébert, C.-A.; Shin, H. S.; Clarke, S.; Borkiewicz, O.; Chapman, K. W.; Seshadri, R.; Cho, J.; Grey, C. P. Multiple Redox Modes in the

Reversible Lithiation of High-Capacity, Peierls-Distorted Vanadium Sulfide. *J. Am. Chem. Soc.* **2015**, *137*, 8499–8508.

(10) Doan-Nguyen, V. V. T. et al. Molybdenum Polysulfide Chalcogels as High-Capacity, Anion-Redox-Driven Electrode Materials for Li-Ion Batteries. *Chem. Mater.* **2016**, *28*, 8357–8365.

(11) Shyam, B.; Chapman, K. W.; Balasubramanian, M.; Klingler, R. J.; Srajer, G.; Chupas, P. J. Structural and Mechanistic Revelations on an Iron Conversion Reaction from Pair Distribution Function Analysis. *Angew. Chem. Int. Ed.* **2012**, *51*, 4852–4855.

(12) Wiaderek, K. M.; Borkiewicz, O. J.; Castillo-Martinez, E.; Roberts, R.; Pereira, N.; Amatucci, G. G.; Grey, C. P.; Chupas, P. J.; Chapman, K. W. Comprehensive Insights into the Structural and Chemical Changes in Mixed-Anion FeOF Electrodes by Using Operando PDF and NMR Spectroscopy. *J. Am. Chem. Soc.* **2013**, *135*, 4070–4078.

(13) Wiaderek, K. M.; Borkiewicz, O. J.; Pereira, N.; Ilavsky, J.; Amatucci, G. G.; Chupas, P. J.; Chapman, K. W. Mesoscale Effects in Electrochemical Conversion: Coupling of Chemistry to Atomic-and Nanoscale Structure in Iron-Based Electrodes. *J. Am. Chem. Soc.* **2014**, *136*, 6211–6214.

(14) Preto, S. K.; Tomczuk, Z.; von Winbush, S.; Roche, M. R. Reactions of FeS_2, CoS_2, and NiS_2 Electrodes in Moleten LiCl−KCl Electrolytes. *J. Electrochem. Soc.* **1983**, *130*, 264–273.

(15) Masset, P. J.; Guidotti, R. A. Thermal Activated ("Thermal") Battery Technology Part IIIa: FeS_2 Cathode Material. *J. Power Sources* **2008**, *177*, 595–609.

(16) Brec, R.; Dugast, A.; Le Mehaute, A. Chemical and Electrochemical Study of the Li_xFeS_2 Cathodic System ($0 < x \leq 2$). *Mater. Res. Bull.* **1980**, *15*, 619–625.

(17) Le Mehaute, A.; Brec, R.; Dugast, A.; Rouxel, J. The Li_xFeS_2 Electrochemical System. *Solid State Ionics* **1981**, *3–4*, 185–189.

(18) Shao-Horn, Y.; Osmialowski, S.; Horn, Q. C. Nano-FeS_2 for Commercial Li/FeS_2 Primary Batteries. *J. Electrochem. Soc.* **2002**, *149*, A1499–A1502.

(19) Shao-Horn, Y.; Osmialowski, S.; Horn, Q. C. Reinvestigation of Lithium Reaction Mechanism is FeS_2 Pyrite at Ambient Temperature. *J. Electrochem. Soc.* **2002**, *149*, A1547–A1555.

(20) Yersak, T. A.; Machpherson, H. A.; Kim, S. C.; Le, V.-D.; Kang, C. S.; Son, S.-B.; Kim, Y.-H.; Trevey, J. E.; Oh, K. H.; Stoldt, C.; Lee, S.-H. Solid State Enabled Reversible Four Electron Storage. *Adv. Energy Mater.* **2013**, *3*, 120–127.

(21) Evans, T.; Piper, D. M.; Kim, S. C.; Han, S. S.; Bhat, V.; Oh, K. H.; Lee, S.-H. Ionic Liquid Enabled FeS_2 for High-Energy-Density Lithium-Ion Batteries. *Adv. Energy Mater.* **2014**, *26*, 7386–7392.

(22) Batchelor, R. J.; Einstein, F. W. B.; Jones, C. H. W.; Fong, R.; Dahn, J. R. Crystal Structure of Li_2FeS_2. *Phys. Rev. B* **1988**, *37*, 3699–3702.

(23) Blandeau, L.; Ouvrard, G.; Calage, Y.; Brec, R.; Rouxel, J. Transition-metal Dichalcogenides from Disintercalation Process. Crystal Structure Determination and Mössbauer Study of Li_2FeS_2 and its Disintercalates Li_xFeS_2 ($0.2 \leq x \leq 2$). *J. Phys. C: Solid State Phys.* **1987**, *20*, 4271–4281.

(24) Totir, D. A.; Bae, I. T.; Hu, Y.; Antonio, M. R.; Stan, M. A.; Scherson, D. A. In Situ Fe *K*-Edge X-ray Absorption Fine Structure of a Pyrite Electrode in a Li/Polyethylene Oxide($LiClO_4$)/FeS_2 Battery Environment. *J. Phys. Chem.* **1997**, *101*, 9751–9756.

(25) Strauss, E.; Calvin, S.; Mehta, H.; Golodnitsky, D.; Greenbaum, S. G.; denBoer, M. L.;

Dusheiko, V.; Peled, E. X-ray Absorption Spectroscopy of Highly Cycled Li/Composite Polymer Electrolyte/FeS_2 Cells. *Solid State Ionics* **2003**, *164*, 51–63.

(26) Jones, C. H. W.; Kovacs, P. E.; Sharma, R. D.; McMillan, R. S. Iron-57 Mössbauer Spectroscopy of Reduced Cathodes in the Lithium/Iron Disulfide Battery System: Evidence for Superparamagnetism. *J. Phys. Chem.* **1990**, *94*, 832–836.

(27) Tryk, D. A.; S. Kim, Y. H.; Scherson, W. X. D. A.; Antonio, M. R.; Leger, V. Z.; Blomgren, G. E. Electrochemical Insertion of Lithium into Pyrite from Nonaqueous Electrolytes at Room Temperature: An *in situ* Fe *K*-Edge X-ray Absorption Fine Structure Study. *J. Phys. Chem.* **1995**, *99*, 3732–3735.

(28) Fong, R.; Jones, C. H. W.; Dahn, J. R. A Study of Pyrite-Based Cathodes for Ambient Temperature Lithium Batteries by *In Situ* ^{57}Fe Mössbauer Spectroscopy. *J. Power Sources* **1989**, *26*, 333–339.

(29) Fong, R.; Dahn, J. R.; Jones, C. H. W. Electrochemistry of Pyrite-Based Cathodes for Ambient Temperature Lithium Batteries. *J. Electrochem. Soc.* **1989**, *136*, 3206–3210.

(30) Totir, D. A.; Antonio, M. R.; Schilling, P.; Tittsworth, R.; Scherson, D. A. In Situ Sulfur *K*-Edge X-ray Absorption Near Edge Structure of an Embedded Pyrite Particle Electrode in a Non-Aqueous Li^+-Based Electrolyte Solution. *Electrochim. Acta* **2002**, *47*, 3195–3200.

(31) Gard, P.; Sourisseau, C.; Ouvrard, G.; Brec, R. Infrared Study of Lithium Intercalated Phases in the Li_xFeS_2 System ($0 \leq x \leq 2$). Characterization of a New Iron Disulfide. *Solid State ionics* **1986**, *20*, 231–238.

(32) Pickard, C. J.; Needs, R. J. High-Pressure Phases of Silane. *Phys. Rev. Lett.* **2006**, *97*, 045504.

(33) Pickard, C. J.; Needs, R. J. *Ab Initio* Random Structure Searching. *J. Phys.: Condens. Matter* **2011**, *23*, 053201.

(34) Clark, S. J.; Segall, M. D.; Pickard, C. J.; Hasnip, P. J.; Probert, M. J.; Refson, K.; Payne, M. First Principles Methods Using CASTEP. *Z. Kristall.* **2005**, *220*, 567–570.

(35) Perdew, J. P.; Burke, K.; Ernzerhof, M. Generalized Gradient Approximation Made Simple. *Phys. Rev. Lett.* **1996**, *77*, 3865–3868.

(36) Monkhorst, H. J.; Pack, J. D. Special Points for Brillouin-Zone Integrations. *Phys. Rev. B* **1976**, *13*, 5188–5192.

(37) Aydinol, M. K.; Kohan, A. F.; Ceder, G.; Cho, K.; Joannopoulos, J. *Ab Initio* Study of Lithium Intercalation in Metal Oxides and Metal Dichalcogenides. *Phys. Rev. B* **1997**, *56*, 1354–1365.

(38) Dudarev, S. L.; Botton, G. A.; Savrasov, S. Y.; Humphreys, C. J.; Sutton, A. P. Electron-Energy-Loss Spectra and the Structural Stability of Nickel Oxide: An LSDA+U Study. *Phys. Rev. B* **1998**, *57*, 1505–1509.

(39) Aras, M.; etin Kl, Combined Hybrid Functional and DFT+U Calculations for Metal Chalcogenides. *J. Chem. Phys.* **2014**, *141*, 044106.

(40) Nakamura, K.; Akiyama, T.; Ito, T.; Freeman, A. J. Half-Metallicity at Ferromagnetic/Antiferromagnetic Interfaces in Zincblende Transition-Metal Chalcogenides: A Full-Potential Linearized Augmented Plane-Wave Study within LDA+U. *J. Appl. Phys.* **2008**, *103*, 07C901.

(41) Yu, L.; Lany, S.; Kykyneshi, R.; Jieratum, V.; Ravichandran, R.; Pelatt, B.; Altschul, E.; Platt, H. A. S.; Wager, J. F.; Keszler, D. A.; Zunger, A. Iron Chalcogenide Photovoltaic Absorbers. *Adv. Energy Mater.* **2011**, *1*, 748–753.

(42) Badrudin, F. W.; Taib, M. F. M.; Hassan, O. H.; Yahya, M. Z. A. Effect of Lithium Intercalation on the Structural and Electronic Properties of Layered $LiFeSO_4OH$ and Layered $FeSO_4OH$ Using First-Principle Calculations. *Comput. Mater. Sci.* **2016**, *119*, 144–151.

(43) Thompson, A.; Attwood, D.; Gullikson, E.; Howells, M.; Kim, K.-J.; Kirz, J.; Kortright, J.; Lindau, I.; Pianetta, P.; Robinson, A.; Scofield, J.; Underwood, J.; Vaughan, D.; Williams, G.; Winick, H. X-ray Data Booklet, (Lawrence Berkeley National Lab, Berkeley, 2009) 1–2.

(44) Ravel, B.; Newville, M. ATHENA, ARTEMIS, HEPHAESTUS: Data Analysis for X-ray Absorption Spectroscopy Using IFEFFIT. *J. Synchrotron Radiat.* **2005**, *12*, 537–541.

(45) Borkiewicz, O. J.; Shyam, B.; Wiaderek, K. M.; Kurtz, C.; Chupas, P. J.; Chapman, K. W. The AMPIX Electrochemical Cell: a Versatile Apparatus for *In Situ* X-ray Scattering and Spectroscopic Measurements. *J. Appl. Crystallogr.* **2012**, *45*, 1261–1269.

(46) Hammersley, A. P.; Svensson, S. O.; Hanfland, M.; Fitch, A. N.; Hausermann, D. Two-Dimensional Detector Software: From Real Detector to Idealised Image or Two-Theta Scan. *High Pressure Res.* **1996**, *14*, 235–248.

(47) Qui, X.; Thompson, J. W.; Billinge, S. J. L. PDFgetX2: a GUI-Driven Program to Obtain the Pair Distribution Function from X-ray Powder Diffraction Data. *J. Appl. Crystallogr.* **2004**, *37*, 678–678.

(48) Farrow, C. L.; Juhas, P.; Liu, J. W.; Bryndin, D.; Bozin, E. S.; Bloch, J.; Proffen, T.; Billinge, S. J. L. PDFfit2 and PDFgui: Computer Programs for Studying Nanostructure in Crystals. *J. Phys.: Condens. Matter* **2007**, *19*, 335219.

(49) Chapman, K. W.; Lapidus, S. H.; Chupas, P. J. Applications of Principal Component Analysis to Pair Distribution Function Data. *J. Appl. Cryst.* **2015**, *48*, 1619–1626.

(50) Brostigen, G.; Kjekshus, A. Redetermined Crystal Structure of FeS_2-Pyrite. *Acta. Chem. Scand.* **1969**, *23*, 2186–2188.

(51) Jain, A.; Ong, S. P.; Hautier, G.; Chen, W.; Richards, W. D.; Dacek, S.; Cholia, S.; Gunter, D.; Skinner, D.; Ceder, G.; Persson, K. A. The Materials Project: A Materials Genome Approach to Accelerating Materials Innovation. *APL Mater.* **2013**, *1*, 011002.

(52) Barrett, C. S. X-ray Study of the Alkali Metals at Low Temperatures. *Acta Cryst.* **1956**, *9*, 671–677.

(53) Loschen, C.; Carrasco, J.; Neyman, K. M.; Illas, F. First-Principles $\mathrm{LDA} + \mathrm{U}$ and $\mathrm{GGA} + \mathrm{U}$ Study of Cerium Oxides: Dependence on the Effective U Parameter. *Phys. Rev. B* **2007**, *75*, 035115.

(54) Boesenberg, U.; Marcus, M. A.; Shukla, A. K.; Yi, T.; McDermott, E.; Teh, P. F.; Srinivasan, M.; Moewes, A.; Cabana, J. Asymmetric Pathways in the Electrochemical Conversion Reaction of NiO as Battery Electrode with High Storage Capacity. *Sci. Rep.* **2014**, *4*, 7133.

(55) Kostov, S.; denBoer, M.; Strauss, E.; Golodnitsky, D.; Greenbaum, S. G.; Peled, E. X-ray Absorption Fine Structure Studies of FeS_2 Cathodes in Lithium Polymer Electrolyte Batteries. *J. Power Sources.* **1999**, *81–82*, 709–714.

(56) Lytle, F. W.; Greegor, R. B. Discussion of X-Ray Absorption Near-Edge Structure: Application to Cu in the High-T_c Superconductors $La_{1.8}Sr_{0.2}CuO_4$ and $YBa_2Cu_3O_7$. *Phys. Rev. B* **1988**, *37*, 1550–1563.

(57) Szymański, J. The Crystal Structure of High-Temperature $CuFe_2S_3$. *Z. Kristallogr. - Cryst. Mater.* **1974**, *140*, 240–248.

(58) McDowell, M. T.; Lu, Z.; Koski, K. J.; Yu, J. H.; Zheng, G.; Cui, Y. In Situ Observation

of Divergent Phase Transformations in Sulfide Nanocrystals. *Nano Lett.* **2015**, *15*, 1264–1271.

(59) Page, K.; Proffen, T.; Terrones, H.; Terrones, M.; Lee, L.; Yang, Y.; Stemmer, S.; Seshadri, R.; Cheetham, A. K. Direct Observation of the Structure of Gold Nanoparticles by Total Scattering Powder Neutron Diffraction. *Chem. Phys. Lett.* **2004**, *393*, 385–388.

(60) Tucker, M. G.; Keen, D. A.; Dove, M. T.; Goodwin, A. L.; Hui, Q. RMCProfile: Reverse Monte Carlo for Polycrystalline Materials. *J. Phys.: Condens. Matter* **2007**, *19*, 335218.

(61) Masset, P. J.; Guidotti, R. A. Thermal Activated ("Thermal") Battery Technology Part IIIb: Sulfur and Oxide-based Cathode Materials. *J. Power Sources* **2008**, *178*, 456–466.

Graphical TOC Entry

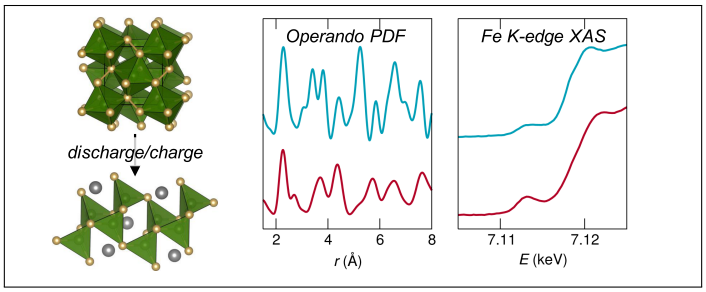

Local Structure Evolution and Modes of Charge Storage in Secondary Li–FeS_2 Cells

Megan M. Butala,[*,†] Martin Mayo,[‡] Vicky V. T. Doan-Nguyen,[¶] Margaret A. Lumley,[†,§] Claudia Göbel,[†] Kamila M. Wiaderek,[‖] Olaf J. Borkiewicz,[‖] Karena W. Chapman,[‖] Peter J. Chupas,[‖] Mahalingam Balasubramanian,[‖] Geneva Laurita,[†] Sylvia Britto,[⊥] Andrew J. Morris,[*,‡] Clare P. Grey,[*,⊥] and Ram Seshadri[*,†,§]

†*Mitsubishi Chemical Center for Advanced Materials, Materials Department, and Materials Research Laboratory, University of California, Santa Barbara, CA 93106, United States*

‡*Theory of Condensed Matter Group, Cavendish Laboratory, University of Cambridge, Cambridge CB3 0HE, United Kingdom*

¶*California NanoSystems Institute, University of California, Santa Barbara, CA 93106, United States*

§*Department of Chemistry and Biochemistry, University of California, Santa Barbara, CA 93106, United States*

‖*X-ray Science Division, Advanced Photon Source, Argonne National Laboratory, Argonne, IL 60439, United States*

⊥*Department of Chemistry, University of Cambridge, Cambridge CB2 1EW, United Kingdom*

E-mail: mbutala@umail.ucsb.edu; ajm255@cam.ac.uk; cpg27@cam.ac.uk; seshadri@mrl.ucsb.edu

Supporting Information

Generation of pseudopotentials for CASTEP

Pseudopotentials were generated by the CASTEP on-the-fly generator using the following parameters: Li: `1|1.0|11|16|16|10U:20(qc=7)`

Fe: `3|2.2|2.0|1.0|8|8|11|40:41:32(qc=5.5)` S: `3|1.8|3|6|6|30:31:32`

Supporting figures

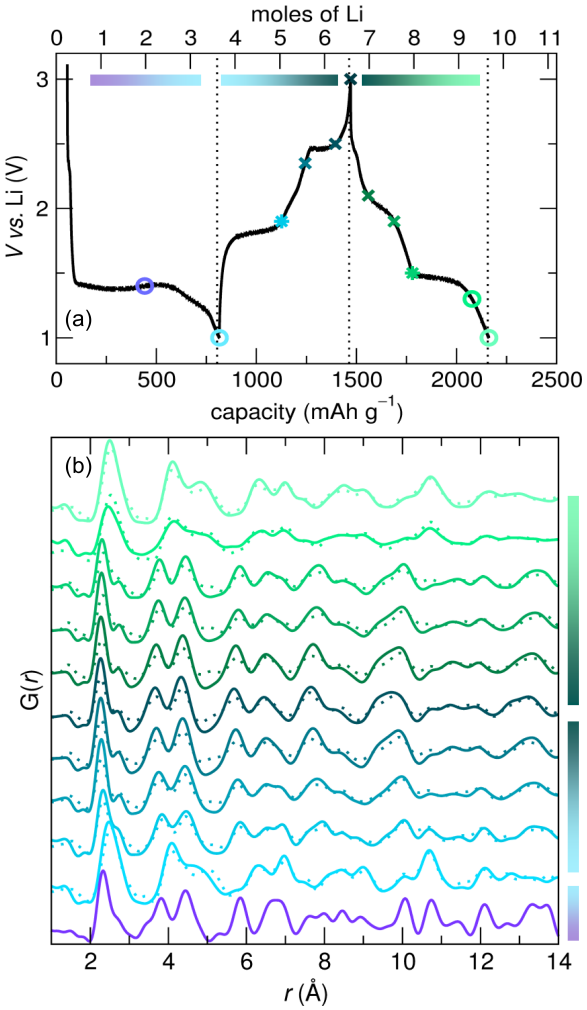

Figure S1: (a) *Ex-situ* discharge-charge curves for 1.5 cycles of FeS_2 marked at the potentials and capacities at which cells were stopped for *ex-situ* PDF. (b) *Ex-situ* PDF at various states of charge are shown as dotted lines with *operando* PDF at similar states of charge shown as solid lines. Only *operando* PDF was measured halfway through the first discharge. *Operando* and *ex-situ* data are in good agreement.

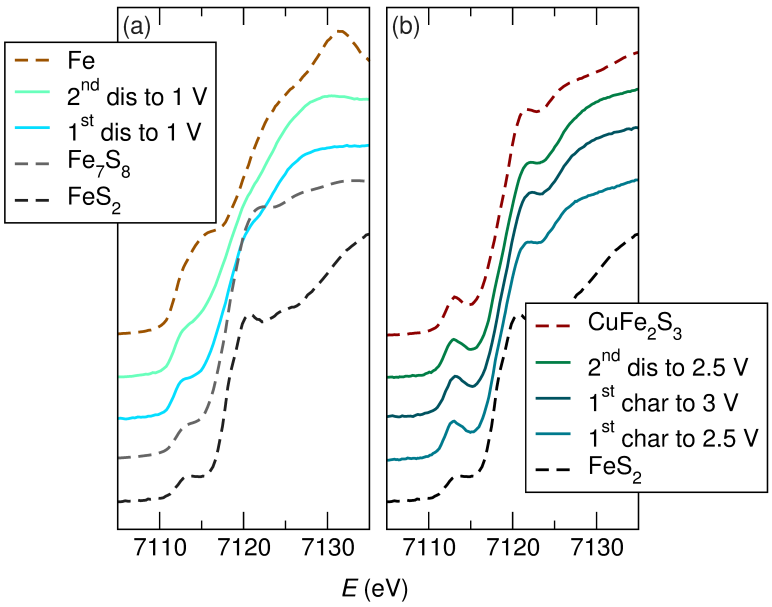

Figure S2: Select Fe *K*-edge XANES highlight the nature of the edge and pre-edge peaks of (a) the discharge products and several standards and (b) charge and near-charge products and ternary $CuFe_2S_3$ ($F\bar{4}3m$) with a pre-edge peak that corresponds to tetrahedrally-coordinated Fe.

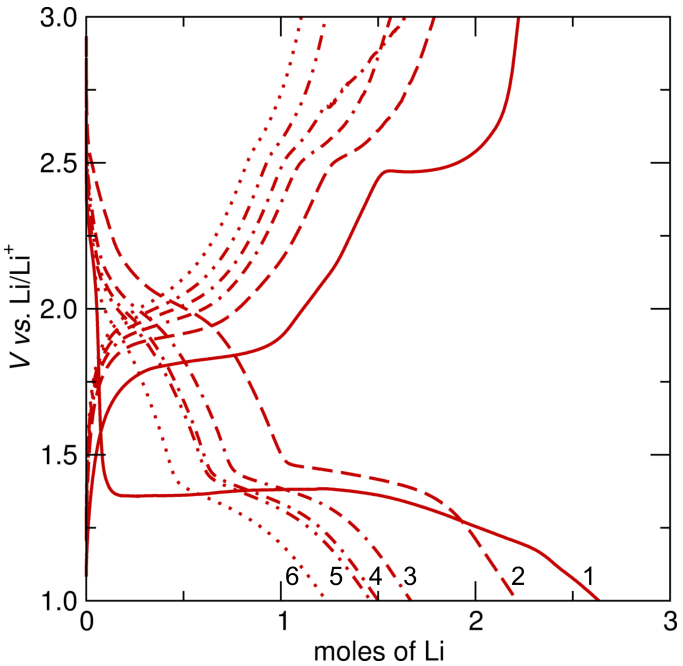

Figure S3: *Operando* galvanostatic cycling in an AMPIX cell is similar to cycling in loose-powder Swagelok cells. Increasingly broken lines correspond to later cycles, as labeled.

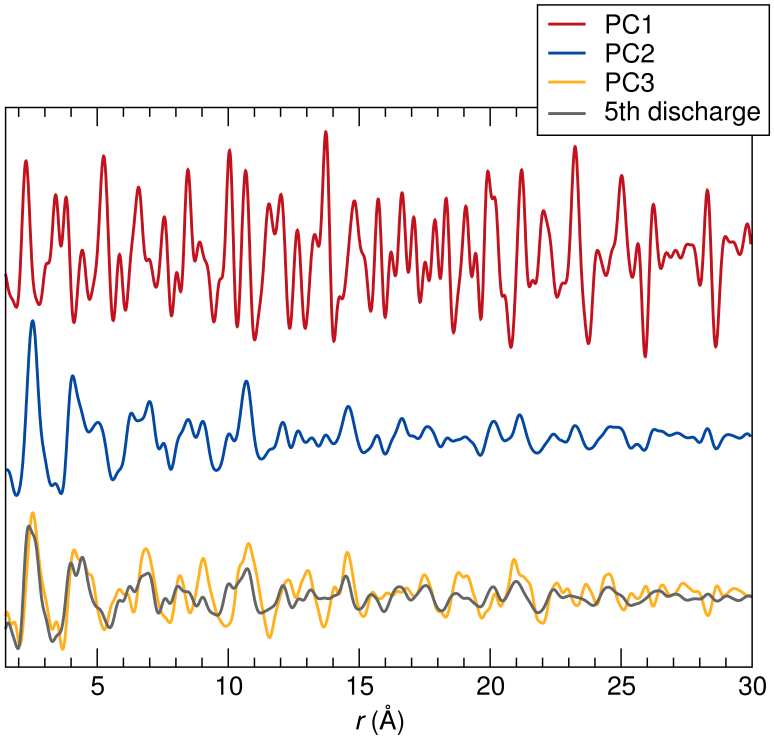

Figure S4: By PCA, three PCs were identified. The principle components underwent transformation to satisfy the necessary criteria and resulted in the three PCs here.[1] PC1 is representative of the PDF collected before cycling of FeS_2 in the composite cathode used in *operando* scattering. PC2 is representative of the first discharge product, which resembles a combination of disordered Fe clusters and Li_2S. PC3 forms intermediately; while there is no clear structure to which this can be assigned, it has some features in common with the fifth discharge product, which is also shown.

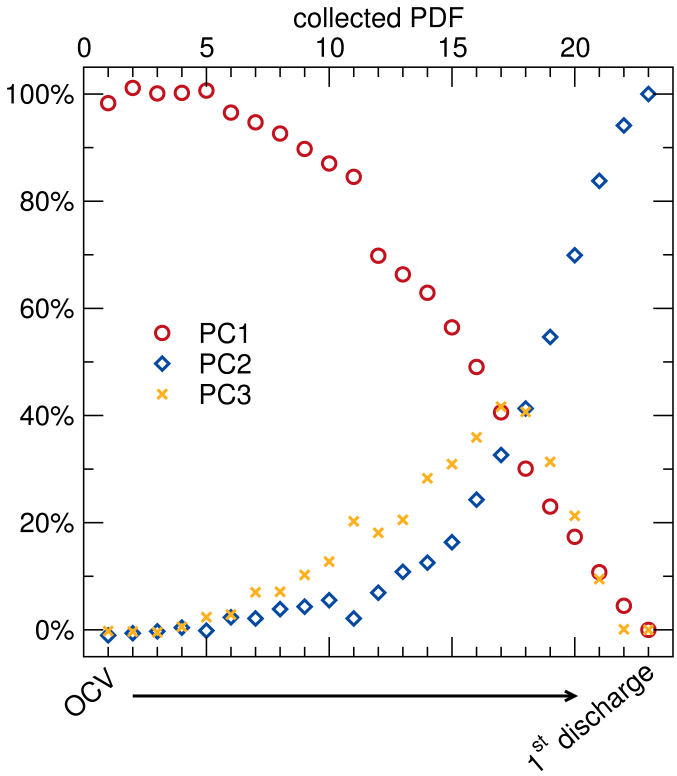

Figure S5: The percent of the identified PCs (shown in Figure S4) in each PDF collected during the first discharge was determined by linear combination analysis. This shows that PC2 and PC3 begin to form early in the discharge at the expense of PC1 (FeS_2). As the end of the discharge is approached, PC1 and PC3 are both consumed in favor of PC2.

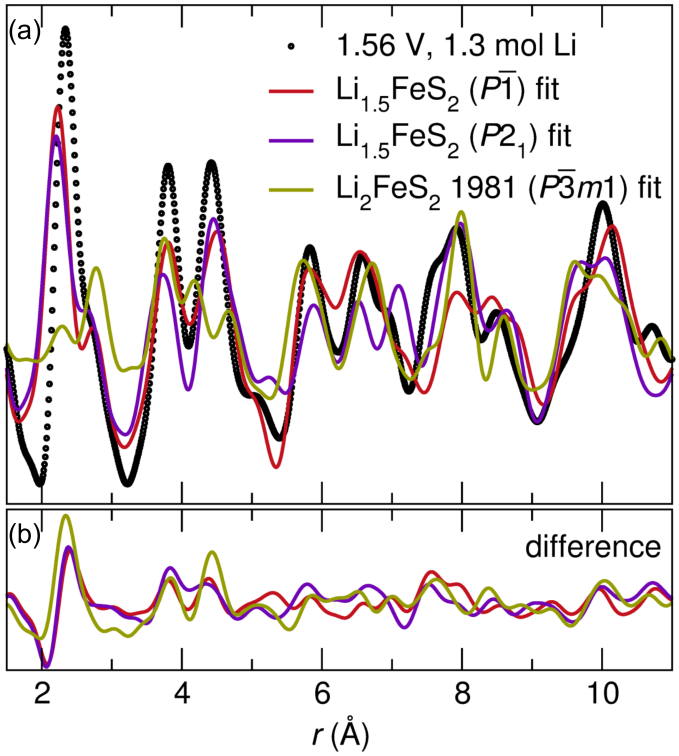

Figure S6: (a) *Operando* PDF at 1.56 V and 1.3 mol Li during the second discharge and fits of several Li−Fe−S ternaries and (b) the difference curves between the measured and fit PDF. $P\bar{1}$ $Li_{1.5}FeS_2$ has a combination of edge- and corner-sharing FeS_4 tetrahedra and $P2_1$ $Li_{1.5}FeS_2$ has chains of edge-sharing FeS_4 tetrahedra. Published Li_2FeS_2,[2] with Li between layers FeS_6 octahedra is not well-fit to the intermediate cycling products. The calculated structures with tetrahedrally-coordinated Fe are in much better agreement with the local structure of the intermediate cycling product.

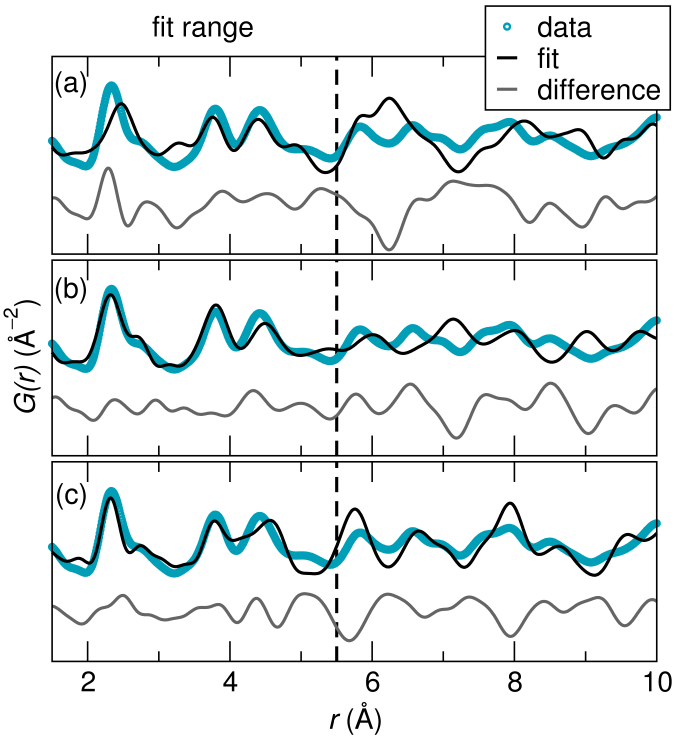

Figure S7: Fits of published ternary intermediate phases to PDF measured about halfway through the second discharge, at a potential of 1.74 V and 1.2 mol Li. Fitting was performed in the range of 1.5 Å to 5.5 Å and then applied to higher r for (a) Li_2FeS_2 ($P\bar{3}m1$) with Li between layers FeS_6 octahedra,[2] (b) Li_2FeS_2 ($P\bar{3}m1$) with Li between layers of mixed occupancy LiS_4 or FeS_4 tetrahedra,[3] and (c) $Li_{1.77}Fe_{1.17}S_2$ ($P3$) with mixed and partial occupancy LiS_4 and FeS_4 corner-sharing tetrahedra.[4]

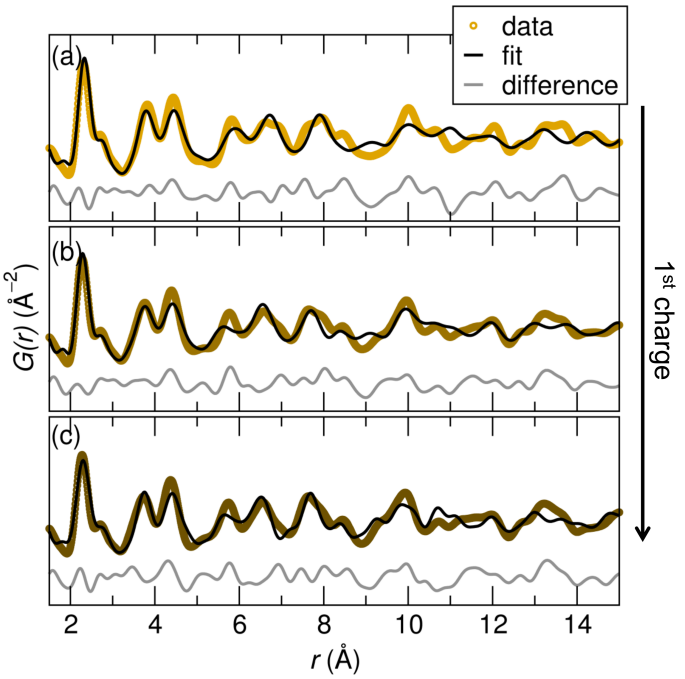

Figure S8: *Operando* PDF at various states of charge during the first charge are fit to $Li_{1.5}FeS_2$ with $P\bar{1}$ symmetry (calculated with $+U$, described in the text) between 1.5 Å and 15 Å. Fit at (a) 2.0 V with 1.4 mol Li, (b) 2.45 V with 1 mol Li, and (c) 2.49 V with 0.7 mol Li.

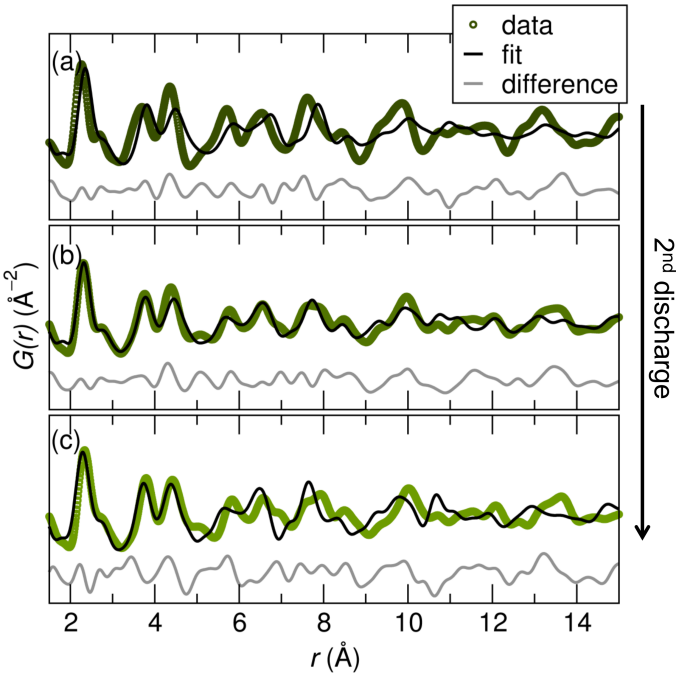

Figure S9: *Operando* PDF at various states of charge during the second discharge are fit to calculated $Li_{1.5}FeS_2$ with $P\bar{1}$ symmetry (calculated with $+U$, described in the text) between 1.5 Å and 15 Å. Fits were carried out for *operando* PDFs collected at (a) 2.9 V with 0.3 mol Li, (b) 2.0 V with 0.8 mol Li, and (c) 1.7 V with 1.2 mol Li.

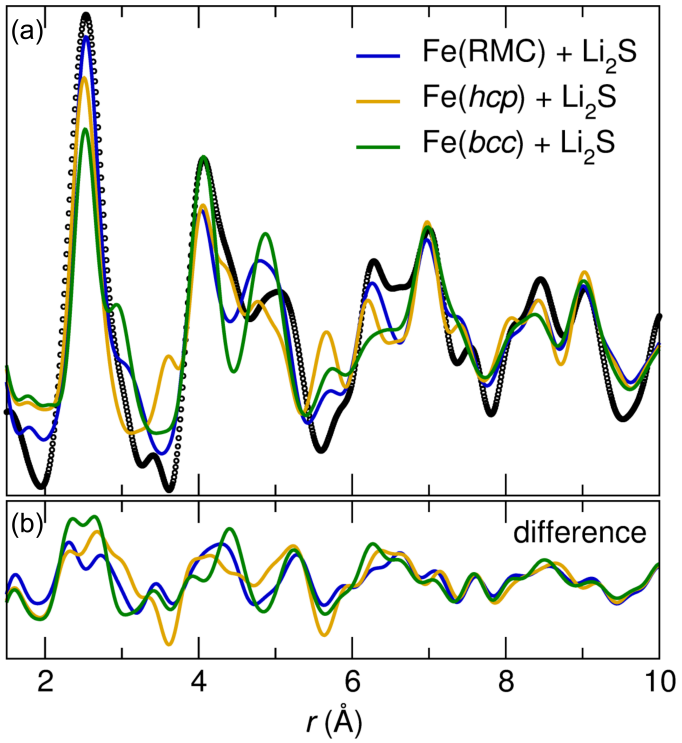

Figure S10: (a) Two-phase fits of the local structure of the first *operando* discharge product to Fe and Li_2S and (b) difference curves. Data is shown as black circles and fits and difference curves as solid lines. Fe with a cluster size of 10 Å was used for each fit. The data is best fit by Li_2S and Fe from the RMC relaxation of a supercell of *bcc* Fe. The *hcp* Fe has strong peaks near 3.6 Å and 5.6 Å that are not observed by experiment. The *bcc* Fe has fewer extra peaks than *hcp*, but is missing a peak near 6.3 Å that is captured by the RMC and *hcp* Fe.

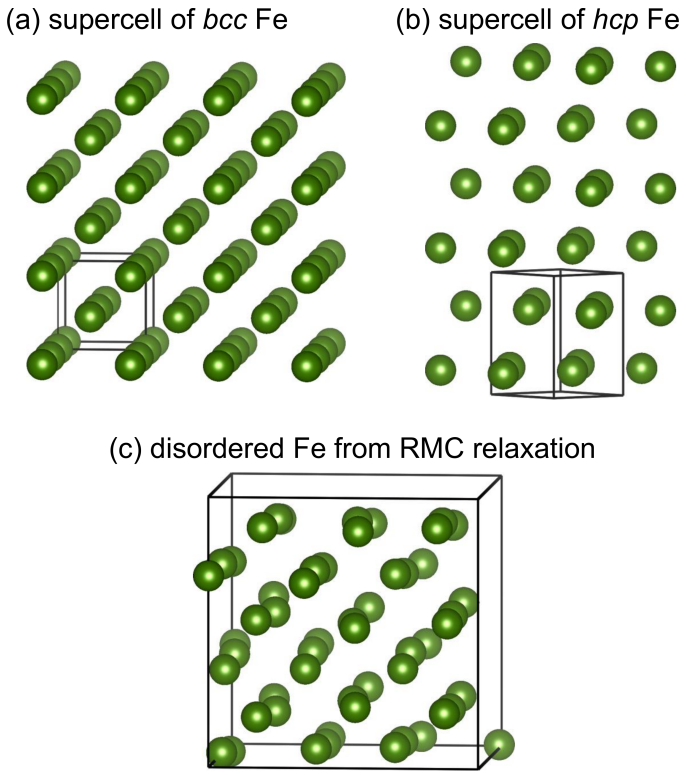

Figure S11: (a) 3×3×3 unit cells of equilibrium $Im\bar{3}m$ (*bcc*) Fe (crystal information file from ICSD entry 52258).[5] (b) 2.5×2.5×3 unit cells of $P6_3mmc$ (*hcp*) Fe (crystal information file from ICSD entry 53450).[6] (c) Disordered Fe generated using a 3×3×3 supercell of *bcc* Fe.

Key structures obtained from DFT calculations

$LiFeS_2$ SG: $P\bar{3}m1$ (No. 164)			
a = 3.99 Å		c = 5.73411 Å	
Atom	x	y	z
Li	0	0	1/2
Fe	1/3	2/3	0.208540
S	0	0	0

$Li_3Fe_2S_4$ SG: $P2_1$ (unique axis b) (No. 4)			
a = 3.60871 Å	b = 10.22361 Å	c = 8.14752 Å	
β = 90.2370°			
Atom	x	y	z
Li	−0.01444	0.48969	0.50788
Li	0.52850	0.51928	0.00231
Li	0.54040	0.71689	0.26150
S	−0.47887	0.77648	−0.7823
S	0.51400	−0.04010	0.29419
S	−0.02298	0.73455	0.57317
S	−0.02943	0.05307	0.79297
Fe	0.02220	0.33821	0.20078
Fe	0.52215	0.17110	0.30453

$Li_3Fe_2S_4$ SG: $Pnma$ (No. 62)			
a = 6.43005 Å b = 10.98970 Å c = 9.30163 Å			
Atom	x	y	z
Li	0.11185	0.04685	0.65907
Li	−0.07260	0.25000	0.44085
S	0.24012	0.03662	−0.08562
S	0.09654	0.25000	0.19384
S	0.74801	0.25000	0.89737
Fe	0.03848	0.62733	−0.02574

$Li_3Fe_2S_4$ SG: $P\bar{1}$ (No. 2)			
a = 6.18197 Å b = 6.86717 Å c = 7.24444 Å			
α = 88.7460° β = 78.9811° γ = 83.7310°			
Atom	x	y	z
Li	−0.00645	0.10954	0.69279
Li	0.55401	0.14516	0.13406
Li	0.48490	0.77891	0.41851
S	0.25900	0.10452	0.39975
S	0.78105	0.78105	0.39975
S	0.28204	0.57517	0.18756
S	0.23633	0.17398	−0.07394
Fe	0.63870	0.53797	0.09757
Fe	0.12452	0.30997	0.20030

Li_2FeS_2 SG: $P\bar{1}$ (No. 2)			
a = 3.96672 Å	b = 6.83113 Å	c = 13.10416 Å	
α = 85.0995°	β = 81.3004°	γ = 89.6690°	
Atom	x	y	z
Li	0.47995	0.68424	0.36733
Li	0.81371	0.06046	0.70671
Li	0.50347	0.32082	0.12401
Li	0.20075	−0.05427	0.80701
S	0.28109	0.77264	0.07171
S	0.78817	0.69439	0.19049
S	0.78546	0.69223	0.19049
S	0.71868	0.22544	0.42909
Fe	−0.00398	0.49644	0.15514
Fe	0.10570	0.39526	0.52516

Li_2FeS_2 SG: $P2_1/c$ (No. 14)			
a = 8.84365 Å b = 6.17097 Å c = 15.79670 Å β = 122.0851°			
Atom	x	y	z
Li	0.08541	0.03223	0.31390
Li	0.13631	0.62211	0.45730
Li	0.35499	0.51117	0.75557
Li	0.38459	0.05381	0.84002
S	0.11988	0.22832	0.46259
S	0.12823	0.23590	0.70444
S	0.36016	0.70141	0.89969
S	0.37017	0.72263	0.14207
Fe	0.12684	0.00709	0.58946
Fe	0.37296	0.00842	0.52608

Li_3FeS_2 SG: $P2_1$ (unique axis b) (No. 4)			
a = 6.88134 Å b = 3.94135 Å c = 7.14157 Å β = 110.7542°			
Atom	x	y	z
Li	0.37286	0.08733	0.36901
Li	0.86952	0.58682	0.36917
Li	0.62204	0.08572	0.11932
S	0.00189	0.09516	0.25507
S	0.51151	0.09111	0.75487
Fe	0.09753	0.59916	0.09665

Li_4FeS_2 SG: $P\bar{1}$ (No. 2)			
a = 5.39985 Å	b = 5.60296 Å	c = 13.34497 Å	
α = 95.7806°	β = 95.9308°	γ = 90.2021°	
Atom	x	y	z
Li	0.75019	0.50060	0.00029
Li	0.19222	−0.05245	0.78068
Li	0.13882	0.89729	0.57493
Li	0.35494	0.11316	0.42992
Li	0.75044	−0.00061	−0.00050
Li	0.19497	0.44617	0.78009
Li	0.69843	0.44462	0.78050
Li	0.30557	0.05199	0.22058
S	0.02762	0.27481	0.11017
S	0.41929	0.64579	0.66900
S	0.08535	0.80876	0.33158
S	0.52777	0.77935	0.11022
Fe	0.12388	0.42623	0.56027
Fe	0.66827	0.43257	0.56219

$Li_3Fe_2S_4$ ($+U_{eff}$ = 4 eV, AFM) SG: $P2_1$ (No. 4) (unique axis b)			
a = 3.97156 Å b = 10.61478 Å c = 8.36303 Å β = 91.8619°			
Atom	x	y	z
Li	−0.01487	0.47662	0.51269
Li	0.51620	0.52191	0.00826
Li	0.54928	0.71884	0.24935
S	0.49385	0.77222	−0.06501
S	0.50068	−0.046080	0.30081
S	−0.02524	0.74107	0.56733
S	−0.02353	0.06185	0.79644
Fe	0.01438	0.34857	0.18959
Fe	0.51829	0.16418	0.30933

$Li_3Fe_2S_4$ ($+U_{eff}$ = 4 eV, FM) SG: $P\bar{1}$ (No. 2)			
a = 6.54340 Å	b = 7.35922 Å	c = 7.55214 Å	
α = 91.2080°	β = 93.1476°	γ = 101.5817°	
Atom	x	y	z
Li	0.01461	0.66011	0.15462
Li	0.40516	0.16473	0.10150
Li	0.51334	0.43110	0.80244
S	0.73414	0.38151	0.07531
S	0.24148	0.30522	0.33148
S	0.72449	0.19526	0.57682
S	0.76788	0.87999	0.19085
Fe	0.35944	0.11085	0.53082
Fe	0.87593	0.20182	0.28110

$Li_3Fe_2S_4$ ($+U_{eff}$ = 4 eV, FM) SG: $P2_1$ (No. 4) (unique axis b)			
a = 3.95342 Å b = 10.59700 Å c = 8.35565 Å β = 92.0424°			
Atom	x	y	z
Li	−0.01529	0.48036	0.51162
Li	0.51625	0.52056	0.00913
Li	0.55000	0.71687	0.25506
S	0.49268	0.76923	−0.05772
S	0.50125	−0.04194	0.29858
S	−0.02865	0.74354	0.55753
S	−0.02721	0.05814	0.79375
Fe	0.01804	0.34423	0.18735
Fe	0.51869	0.16818	0.31302

Li_2FeS_2 (Supercell, Model 1) SG: $P3m1$ (No. 156)			
a = 3.90342 Å			c = 12.51164 Å
Atom	x	y	z
Li	0.33333	0.66667	0.17791
Li	0.33333	0.66667	0.67791
Li	0.00000	0.00000	0.00692
S	0.66667	0.33333	0.12747
S	0.33333	0.66667	0.37444
S	0.66667	0.33333	0.62747
S	0.33333	0.66667	0.87444
Fe	0.66667	0.33333	0.31327
Fe	0.66667	0.33333	0.81327

Li_2FeS_2 (Supercell, Model 2) SG: $P\bar{3}m1$ (No. 164)			
a = 3.91053 Å			c = 12.44133 Å
Atom	x	y	z
Li	0.33333	0.66667	0.16871
Li	0.66667	0.33333	0.83129
Li	0.00000	0.00000	0.00000
S	0.66667	0.33333	0.12376
S	0.33333	0.66667	0.37126
S	0.66667	0.33333	0.62874
S	0.33333	0.66667	0.87624
Fe	0.66667	0.33333	0.30858
Fe	0.33333	0.66667	0.69142

References

(1) Chapman, K. W.; Lapidus, S. H.; Chupas, P. J. Applications of principal component analysis to pair distribution function data. *J. Appl. Cryst.* **2015**, *48*, 1619–1626.

(2) Le Mehaute, A.; Brec, R.; Dugast, A.; Rouxel, J. The Li_xFeS_2 Electrochemical System. *Solid State Ionics* **1981**, *3–4*, 185–189.

(3) Batchelor, R. J.; Einstein, F. W. B.; Jones, C. H. W.; Fong, R.; Dahn, J. R. Crystal Structure of Li_2FeS_2. *Phys. Rev. B* **1988**, *37*, 3699–3702.

(4) Blandeau, L.; Ouvrard, G.; Calage, Y.; Brec, R.; Rouxel, J. Transition-metal Dichalcogenides from Disintercalation Process. Crystal Structure Determination and Mössbauer Study of Li_2FeS_2 and its Disintercalates Li_xFeS_2 ($0.2 \leq x \leq 2$). *J. Phys. C: Solid State Phys.* **1987**, *20*, 4271–4281.

(5) Owen, E. A.; Yates, E. L. XLI. Precision Measurements of Crystal Parameters. *Phil. Mag.* **1933**, *15*, 472–488.

(6) Takahashi, T.; Basset, W. A.; Hokwang, M. Isothermal Compression of the Alloys of Iron up to 300 kbar at Room Temperature: Iron-Nickel Alloys. *J. Geophys. Res. B: Solid Earth* **1986**, *73*, 4717–4725.